TECHNISCHE UNIVERSITÄT MÜNCHEN

Investigation of a Navigation-Grade RLG SIMU type iNAV-RQH

R. Dorobantu, C. Gerlach

IAPG / FESG No. 16

Institut für Astronomische und Physikalische Geodäsie
Forschungseinrichtung Satellitengeodäsie

München 2004

Investigation of a Navigation–Grade RLG SIMU type iNAV–RQH

R. Dorobantu, C. Gerlach

IAPG / FESG No. 16

München 2004

ISSN 1437-8280
ISBN 3-934205-15-1

Adressen:
Institut für Astronomische und Physikalische Geodäsie
Technische Universität München
Arcisstrasse 21
D-80290 München
Germany
Telefon: +49-89-289-23190
Telefax: +49-89-289-23178
http://tau.fesg.tu-muenchen.de/

Forschungseinrichtung Satellitengeodäsie
Technische Universität München
Arcisstrasse 21
D-80290 München
Germany
Telefon: +49-89-289-23191
Telefax: +49-89-289-23178
http://tau.fesg.tu-muenchen.de/

Investigation of a Navigation-Grade RLG SIMU type iNAV-RQH

RAUL DOROBANTU AND CHRISTIAN GERLACH

Institut für Astronomische und Physikalische Geodäsie (IAPG), Technische Universität München
D-80290 München, Germany (e-mails: dorobantu@bv.tum.de and gerlach@bv.tum.de)

Table of contents

Investigation of a Navigation-Grade RLG SIMU type iNAV-RQH

1. Introduction

The work presents a characterization and some results from evaluation experiments made with our Ring Laser Gyroscope (**RLG**) navigation grade Strapdown Inertial Measurement Unit (**SIMU**) type iNAV-RQH of the class 1 nmi/h precision. After a short presentation of the principal features of the SIMU, a description of the inertial sensor constructive principles and error models is given. In order to evaluate our strapdown IMU we have conceived laboratory and field tests, performed on a medium-precision turn-table and in the frame of a car-navigation mission, using a **DGPS** (Differential GPS) reference solution (in our case, an On-the-Fly (**OTF**) kinematic **DGPS** solution, delivering accurate position-references at regular epochs of integer seconds). The post-processed 3-D inertial-only or integrated GPS/INS solutions are obtained using the dedicated software Kingspad. A noise and error analysis, with concrete results from laboratory and field tests is presented too. With a position precision in the *sub-dm* domain (differences to the cm-precision DGPS reference trajectory, with 1-σ relative errors of about 1 cm) over driven trajectory perimeters of hundreds of meters, resp. with acceleration errors in *mGal* domain (after appropriate filtering over about 60…100 s) and with attitude errors in *arcsec* range, the RLG SIMU Type iNAV-RQH from iMAR is considered fully suitable for accurate navigation, surveying and precision gravity determinations.
Some preliminary results were already given in *[Dorobantu et al., 2004],* the present extended form including more insides in the sensor technology and error models as well as an indoor INS-navigation experiment with **ZUPT**s (Zero velocity UPdaTes of the Inertial Navigation System). Supplementary experiments, like static tilting, damping-tests or SIMU's statically evaluation, as well as more insight in the **ISA** (Inertial Sensor Assembly), or direct derivation of geodetic parameters from the registered SIMU data, are presented in the appendix.

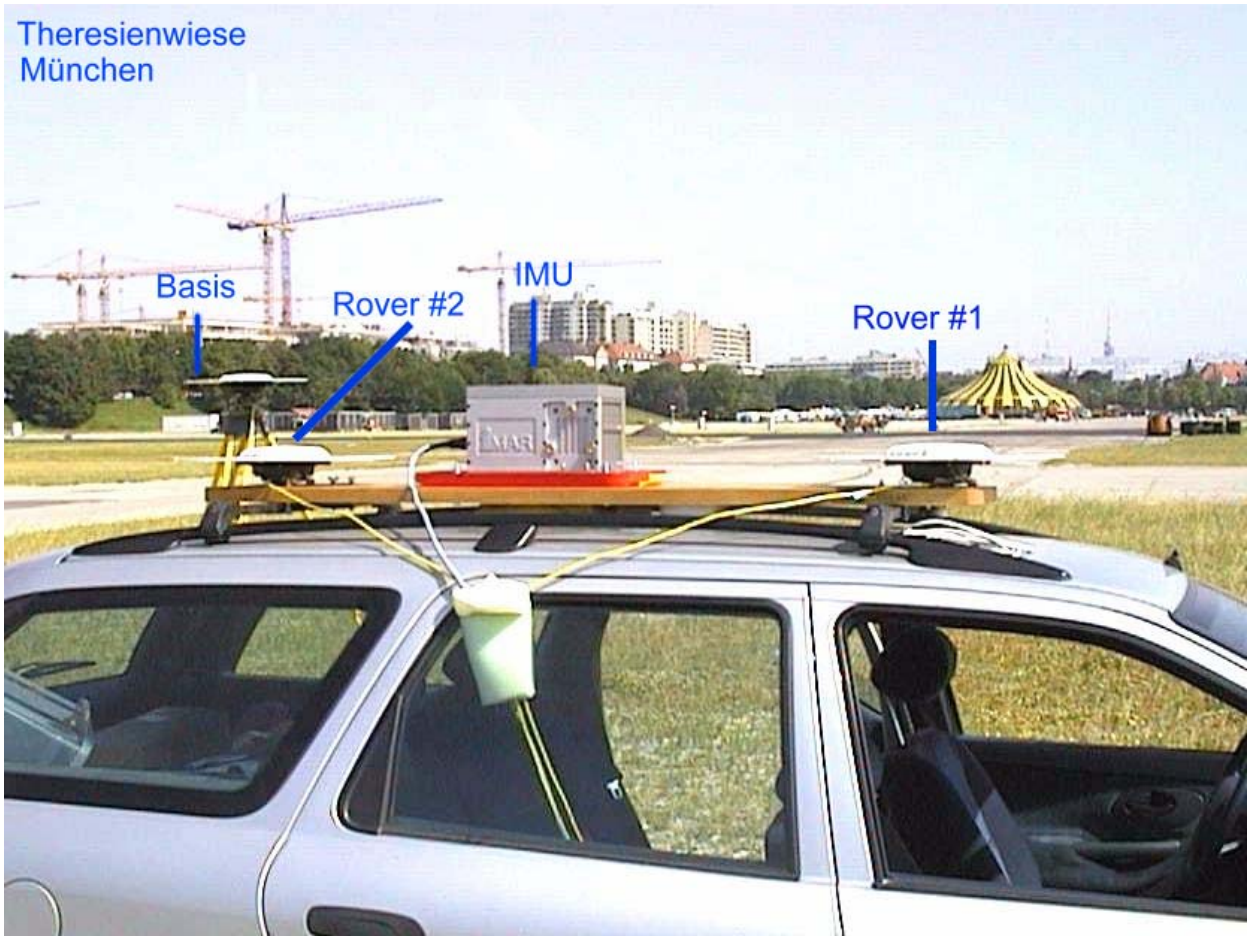

Fig. 1 *DGPS/INS car-experiment in Munich*

Fig. 1 shows the car experiment made in Munich on a terrain with good GPS-satellite visibility (Theresienwiese): one can see the strapdown IMU (a RLG type iNAV-RQH from iMAR) mounted in the middle, between the two rover GPS antennas, as well as the reference basis GPS antenna (all GPS receivers are 18-channel, type Trimble-4000SSI). Without a good understanding of the sensor error models *[Grewal et al., 2000, IEEE Std. 337-1972, IEEE Std. 647-1995, Savage, 1997]* it is not possible to obtain accurate solutions, therefore the following chapter is dedicated to presentation of the inertial sensor technology and their error models.

The post-processing navigation solution analysis, made with Kingspad (originated from the University of Calgary, Dept. of Geomatics) permits a pertinent evaluation of the SIMU and also allows an estimation of sensor parameters. Chapter 3.2.2 illustrates the evaluation made for INS-only solutions (only with ZUPTs) as well as for GPS/INS integration. A short investigation about the precision of the reference GPS solution has also been made by analyzing the GPS relative position errors of the fixed distance between the two rover antennas. Finally, some conclusions from evaluation experiments are presented, with special focus on future hardware improvements and enlarged error models implementation.

1.1. Strapdown-IMU characteristics

The Strapdown navigation-grade IMU iNAV-RQH, characterized by a medium-precision performance, uses a Honeywell inertial sensor cluster, based on three servo-accelerometers type QA2000-40 (selected-ones providing better parameters, such as noise figure, bias and scale factor stability, linearity, acceleration sensitivity) and three new-generation dithered Ring Laser Gyroscopes type GG1320 (also selected for better noise figure).

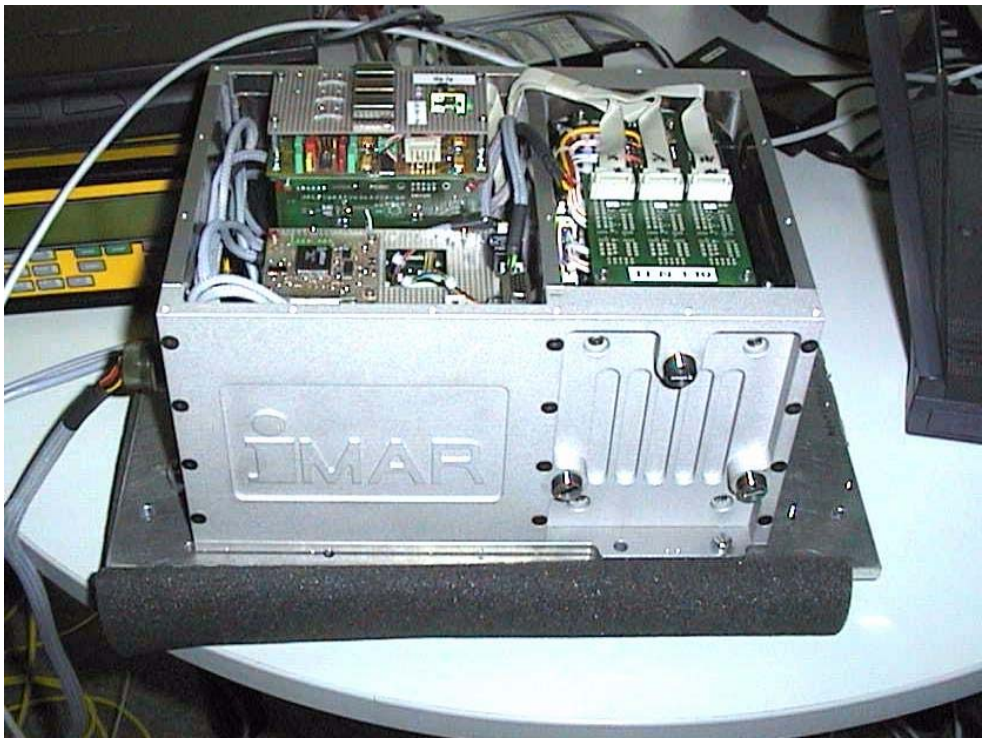

Fig. 2 *Inside-view of the SIMU*

An inside view of the unit's hardware is given in Fig. 2. The inertial sensor assembly, provided with shock-mounts for mechanical protection (that can be clamped, for special experiment purposes), delivers the inertial sensor data via an electronic block of acquisition and pre-processing (anti-aliasing filters, A/D converters of the accelerometer data, provided also with temperature, scale factor, bias and misalignment compensations, etc.). The IMU (see the block-diagram in Fig. 3), controlled by an industry-PC CPU, stores the inertial sensor data (such as the 24-bit converted acceleration data or the digital RLG information) on the internal hard-disk (a 3 GB memory capacity of flash-disk type, chosen to eliminate the potential noise-source); the data are synchronized by means of an internal precision time-basis, that can also be calibrated via the external PPS (pulse per second) GPS receiver signal: the absolute calibration of the time-scale is then achieved through the use of the NMEA-0183 (National Marine Electronics Association) serial-interface signals (the four signals: GGA, GLL, RMC, VTG permit, apart from the time and date information, the receipt of GPS data, such as position and velocity, that can be stored on the IMU in binary files). Supplementary inputs are provided for event marker signals or for auxiliary odometer information. The IMU system software enables the configuration of the unit, by parameter specification, and provides calibration files for the inertial sensor cluster. Such configuration parameters are, among many others: the local position coordinates, the state-variables precisions for the on-line running of Kalman filters for coarse and fine alignments, resulting the Roll, Pitch, Yaw orientation angles (between the SIMU *body*-system and the local-level geodetic reference system). A special feature of this SIMU is the full access to all raw data, being available more than 40 variables: one can access the total uncompensated values (e.g., non-calibrated accelerometer data, without temperature compensations), as well as the fully corrected signals (e.g., the calibrated accelerometer data, compensated also for temperature, gravity and earth rotation rate).

The data, including GPS data or system-status information, can be accessed independently, via connection of an external keyboard and display directly to the IMU, or via an external PC-unit. The bi-lateral communication with the external PC (for navigation purposes often a Notebook), enabling the IMU-control or real-time navigation data display/storage under a RS232 serial interface, uses Windows or DOS programs; a post-mission off-line external data storage is made then via serial communication or Ethernet link (protocols such as IPX, NetBEUI, TCP/IP or Net Use command). The recorded IMU binary data can be used directly, or in a converted ASCII form, as input for navigation post-processing programs.

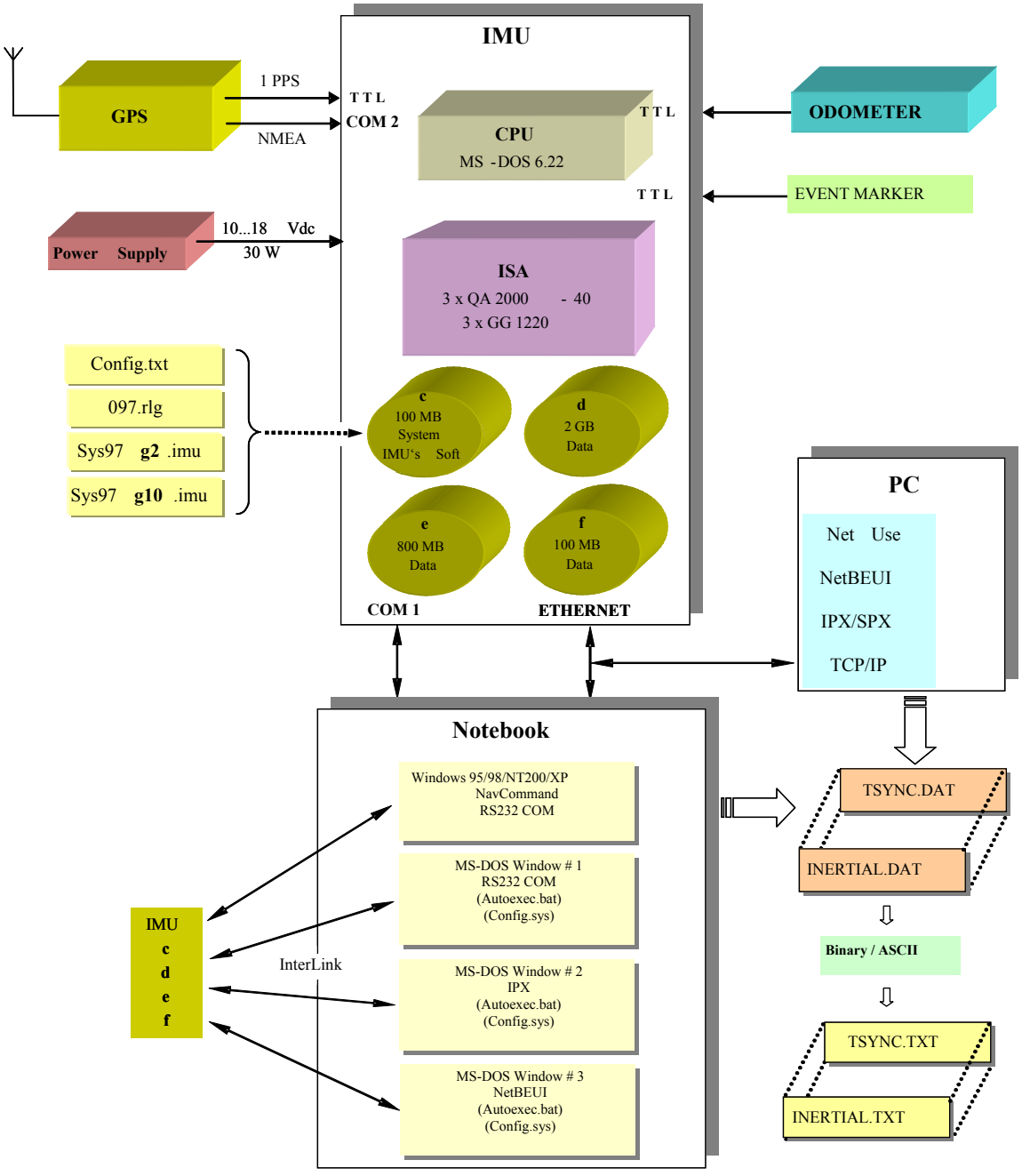

Fig. 3 *SIMU structure and the data-exchange flow*

The SIMU exhibits over further remarkable special features:

- total protection of the supply input
- galvanic separation of IMU accesses
- high acquisition rate (1 kHz now, but very soon 2 kHz, about three times higher then the dithering frequencies)
- electronically switchable accelerometer full-scale range (2g/10g)
- software dithering switch-off (for certain precision experiments).

The principal performance of the SIMU and its sensors are summarized in the Tab. 1 *[from iMAR, 2001]*.

Tab. 1 *Principal performance characteristics of the SIMU type iNAV-RQH from iMAR*

Measurement parameters:	Roll, pitch, yaw, acceleration, velocity, rate, position
	± 500 °/s range
Measurement range:	± 10/10/15 °/s in high precision mode
	± 2 g (acceleration)
Resolution:	1.13 arcsec (quantization)
	0.2 µg
Nonlinearity:	10 ppm (gyro)
	15 µg/g² (accel.)
Scale factor error:	10 ppm (gyro)
	70 ppm (accel.)
Random Walk:	0.0018 deg/sqrt(hr)
Accel. Noise Density:	8 µg/sqrt(Hz)
Bias repeatability:	0.002 deg/hr
	< 15 µg
Sampling rate:	up to 1000 Hz, synchronized to PPS (depends from computation requirements)
Output rate:	1...500 Hz
Latency:	< 1 ms ±10 µs (max)
Data output:	RS232, 115.2 kBd
	(data with time stamp according to XIO-definitions)
Velocity input:	from external odometer
DGPS input:	NMEA input (RS232)
Weight:	< ca. 13 kg
Size:	ca. 350 x 213 x 180 mm
Shock:	60 g, 11 ms
Power supply:	10...18 V DC, protected against wrong polarity and over-voltage up to 40 V DC

2. Inertial sensor technology and error models

The selected highly sensitive QA2000-40 balanced pendulous accelerometers and the dithered GG1320 Laser-gyroscopes (practically not sensitive to acceleration and temperature variations) assure good precision for a navigation-grade SIMU. A detailed insight concerning the principles of that inertial sensors and their errors, which permits a correct data interpretation, is presented in the next three sections.

2.1. Specific-force sensors (accelerometers)

The principle of accelerometers is based on the measurement of the relative displacement that arises between the elastically suspended proof mass and the accelerometer frame subject to acceleration (inertial d'Alembert force) (see the spring-mass and balancing pendulous accelerometer principles in Fig. 4).

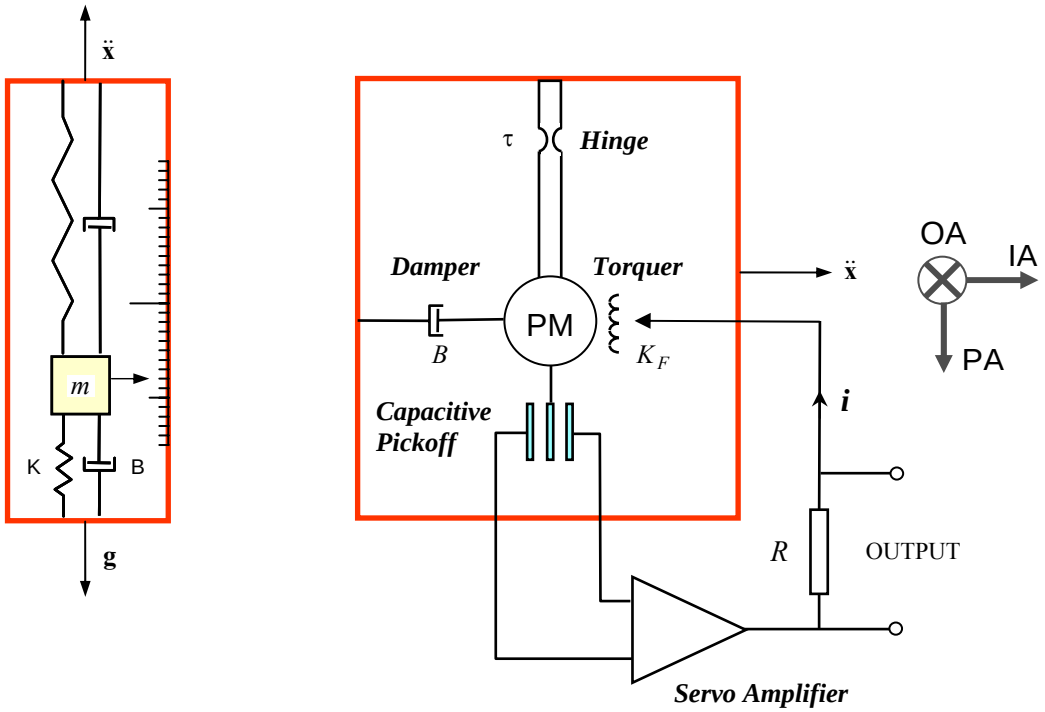

a. *Spring-mass accelerometer* **b.** *Pendulous balancing accelerometer*

Fig. 4 *Accelerometer principles: spring-mass and pendulous balancing accelerometer*

To attain a finite response time of the accelerometer a damped suspension of the proof-mass is used. Accelerations acting in the sensitive axis have the same effect like the static gravity (consequence of the equivalence principle), as shown explicitly in Fig. 4-a for the spring-mass accelerometer.
In contrast to the spring-mass accelerometer, the IMU's pendulous accelerometer QA2000-40 uses an antagonist torque to establish the operating point, produced by an elastic quartz suspension (see Fig. 5, 6) of the proof-mass (PM), which assures a reduced torsion constant. The input axis IA, the pendulous axis PA – situated along the pendular arm – and the output axis OA, perpendicular to the two others, are also depicted in Fig. 4, 5. The accelerometer employs a capacitive pick-off to command the feedback compensation through a linear electrodynamic actuator (Lorentz force), that produces a rebalancing torque. As a consequence of the continuous compensation, the proof-mass pendular amplitude is very small, resulting in a very good linearity and an almost complete lack of hysteresis, with the additional benefit of bias (originating from residual non-elastic moments of the suspension) and drift (caused from material fatigue) reduction. The output current/voltage signal is proportional to the magnitude of the rebalancing torque.

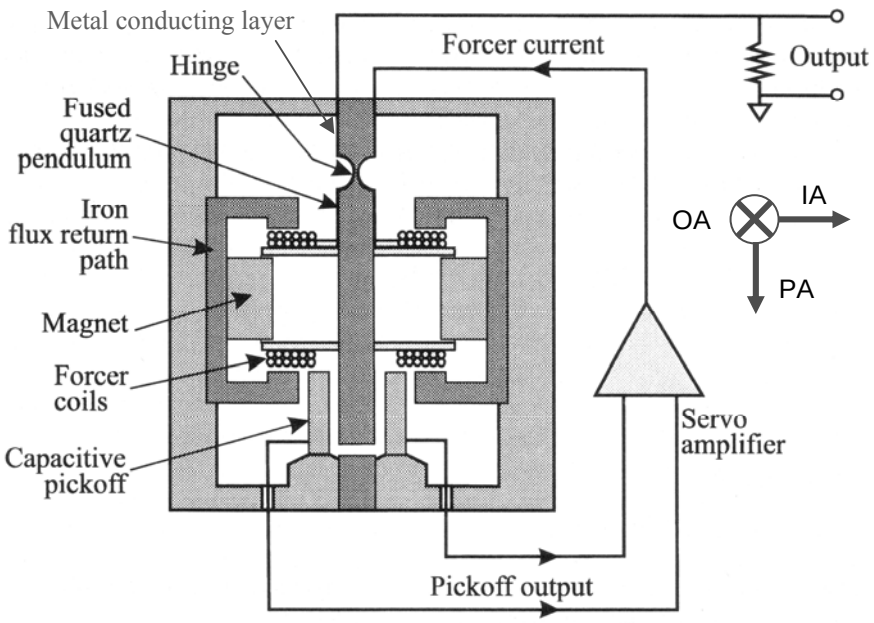

Fig. 5 *Physical realization of the pendulous rebalancing accelerometer Honeywell QA2000 [from Lawrence, 1999]*

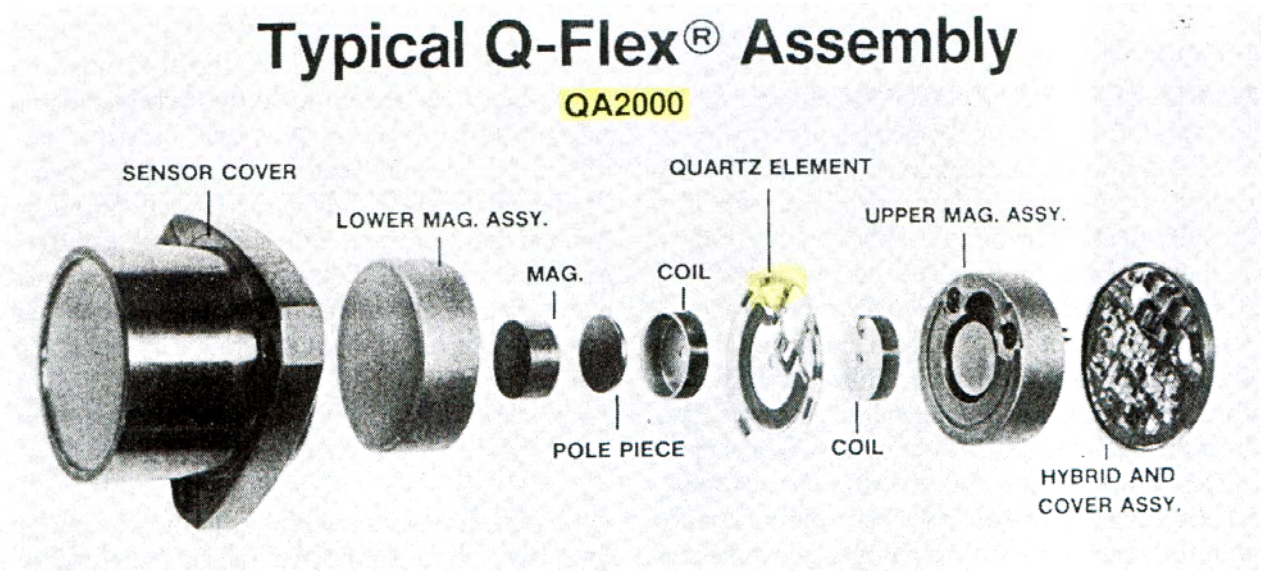

Fig. 6 *Exploded view of the QA2000 Honeywell accelerometer, from [AlliedSignal, 1998]*

The equilibrium of the acting torques – the *active* torque, due to the system acceleration ($M_a = m \cdot a \cdot l_{MC}$, with m the equivalent pendulum mass, concentrated in the centre of mass, and l_{MC} the pendular arm), the *antagonist* one (torsion momentum: $M_\tau = \tau \cdot \theta$, with τ the pendulum elastic restraint and θ the deflection angle of the pendulum-arm with respect to the accelerometer case), the *compensation* torque ($M_r = F_r \cdot l_F$, the product between the torquer rebalance force F_r and the torquer arm l_F) and the damping (*friction)* torque, proportional to the angular rate ($M_f = B \cdot \dot{\theta}$) – permits the formulation of the differential equation for this rotating, oscillating system (using the scalar form of the angular momentum theorem: $\dot{\mathbf{K}} = J \cdot \dot{\boldsymbol{\omega}} = \sum_i \mathbf{M}_i^{ext}$):

$$J \cdot \ddot{\theta} = \sum_i M_i^{ext} \,, \tag{2.1-1}$$

where: J = inertial moment of the pendular arm,

$\sum_i M_i^{ext}$ = the sum of all externally applied torques (see above).

The linearity of the rebalanced sensor is entirely dependent on the high linearity property of the Lorenz-force torquer: $F_r = K_F \cdot i$ (i represents the applied compensation current, with the coefficient $K_F = B_{gap} \cdot l_{coil-wire}$). The

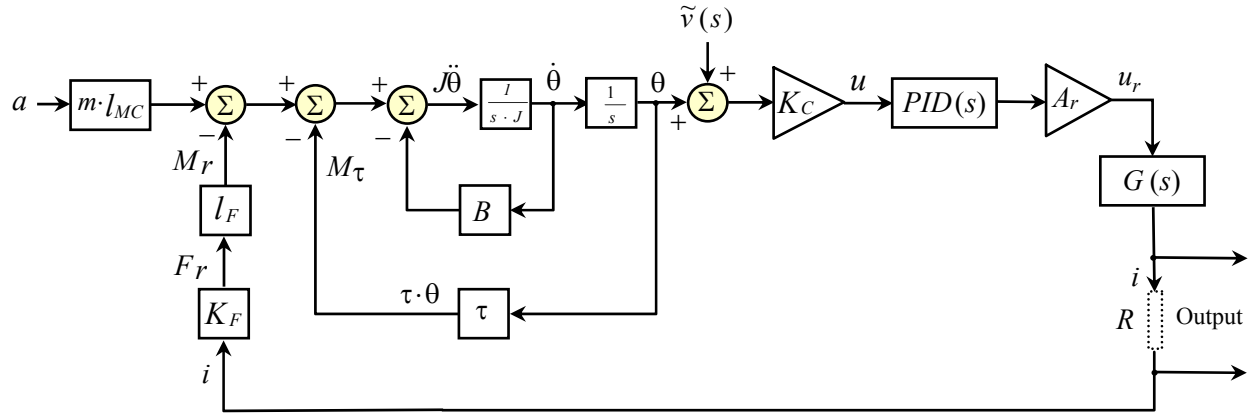

Fig. 7 *Dynamic model of the pendulous accelerometer with magnetic rebalancing*

pendulous-accelerometer block-diagram in Fig. 7, where all the variables are Laplace transforms, shows also the capacitive-detector transfer coefficient K_C, in [V/rad] *[see, e.g., Merhav, 1996]*, the rebalance-loop amplification A_r (both of them considered as frequency-independent terms), respectively the *PID*(s) (Proportional, Integral, Differential) regulator transfer function. In the transfer function *G(s)* the frequency dependent term issues from the electrical model of the balancing coil assembly.

The expressions of transfer-functions in the block-diagram shown in Fig. 6 are:

$\frac{1}{s^2 J + sB + \tau}$: the transfer-function of the accelerometer sensor element, a damped elastic pendulum;

$PID(s) = K_{PID} \cdot \frac{s^2 T_d T_i + sT_i + 1}{sT_i(1 + s\tau_{del})}$: the transfer-function of the lag-compensation element, of type Proportional-Integral-Derivative, with K_{PID} the amplification factor of the *PID*-regulator, T_d and T_i the derivative and the integrating time constants, respectively, and τ_{del} a first-order delay term;

$G(s) = \frac{1}{R + sL}$: the equivalent Laplace admittance for the electric part of the rebalance-torquer assembly, with R the serial resistance (winding resistance neglected) and L the total coils inductivity.

We write the expression of the closed-loop transfer-function, following the above block-diagram, with explicit dependencies from the applied acceleration *a(s)* and from the noise contribution $\tilde{v}(s)$ in the form:

$$u_{out}(s) = F_D(s) \cdot a(s) + F_N(s) \cdot \tilde{v}(s) \,, \tag{2.1-2}$$

that is:

$$u_{out}(s) = \frac{R \cdot m \cdot l_{MC}}{K_F \cdot l_F + \frac{s(s^2 J + sB + \tau)(sT_i\tau_{del} + T_i)(sL + R)}{K_C \cdot K_{PID} \cdot A_r \cdot (s^2 T_d T_i + sT_i + 1)}} \cdot a(s) + \frac{R}{\frac{K_F \cdot l_F}{s^2 J + sB + \tau} + \frac{s(sT_i\tau_{del} + T_i)(sL + R)}{K_C \cdot K_{PID} \cdot A_r \cdot (s^2 T_d T_i + sT_i + 1)}} \cdot \tilde{v}(s)$$

and consider the asymptotic values of the factors F_D and F_N, for the null pulsation ($s = j\omega = 0$), resp. for infinite ones ($s \to \infty$). Then we obtain information in a broad frequency spectrum about the dynamic sensor behavior, respectively about the noise influence:

$$F_D(s)\big|_{s=0} = \frac{R \cdot m \cdot l_{MC}}{K_F \cdot l_F} \tag{2.1-3}$$

$$F_D(s)\big|_{s \to \infty} = 0 \tag{2.1-4}$$

$$F_N(s)\big|_{s=0} = \frac{R \cdot \tau}{K_F \cdot l_F} \tag{2.1-5}$$

$$F_N(s)\big|_{s\to\infty} = 0\,. \tag{2.1-6}$$

One can see the independence of the accelerometer static sensitivity from the sensible-element parameters (relation 2.1-3) and also the noise attenuation with the increasing frequency (relation 2.1-6) due to the filtering effects of the considered constituent blocks.

Tab. 2 *Q-Flex accelerometers QA2000-40 (selected Allied Signal Aerospace)*

Performance	Value
Range	± 25 g
Bias	<4 000 µg
Scale Factor	1.2...1.46 mA/g
Frequency Response (0...300 Hz)	≤ 0.45 dB
Natural Frequency	>800 Hz
Damping Ratio	0.3...0.8
Noise power density	8 µg/sqrt(Hz)
Resolution (dc)	1 µg
2nd Order Nonlinearity	15 µg/g²
Hysteresis	0.006 % FS (60 ppm)
Repeatability	0.003 % FS
Pendulous or Input axis misalignment	<2 mrad
Vibration Rectification Coefficient (0...500 Hz)	10...40 µg/g² rms
Temperature Sensitivity	3...25 µg/°C

An analysis of the Laplace transfer function 2.1-2 (e.g., through Bode diagrams) gives information about the uniformity of the accelerometer transfer-factor in the measurement bandwidth, as well as about the phase linearity in the same domain of interest. The compact accelerometer symmetric construction, with air damping, enables a broad frequency band, with a very good linearity and a small sensitivity to the environmental factors. Using the incorporated temperature-sensor data, one obtains a good correction of the accelerometer output. Table 2 gives the principal technical characteristics of the IMU accelerometers.

2.2. Ring Laser Gyroscopes

Beginning at about 1963, after the *Laser gyroscope* had been demonstrated by Macek and Davis *[Macek et al., 1963]*, the optical gyros trend to become a standard in inertial navigation, especially for *strapdown mechanization*. They provide high dynamics (up to ±1000 °/s), with better insensitivity to mechanical accelerations (for a high-quality strapdown system the gyro *g*-sensitive bias must be smaller than 0.0001 (deg/h)/g), smaller biases and drifts (stability: 0.001 °/h, random walk: 0.003 °/$\sqrt{\text{h}}$), very good scale factor stability (approx. 10 ppm) and negligible gyro scale factor asymmetry (order of 1 ppm) and gyro misalignments (better than 6 arcsec) *[Krempasky, 1999]*. Also the reliability is remarkable, with *MTBF* (Mean Time Between Failures) in the order of $5 \cdot 10^4$ h. Compared to the mechanical gyroscopic sensors, the ring laser gyroscopes are practically insensitive to temperature variations (thermal sensitivities in the order of a fraction of 1 ppm/°C); additionally, they have a quasi-instantaneous initialization time-period (Δt_{init} inferior to 100 ms).

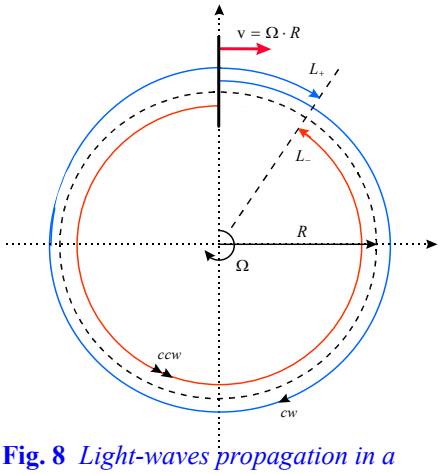

Fig. 8 *Light-waves propagation in a rotating Sagnac interferometer*

The principle of the optical RLG is based on the pure relativistic Sagnac effect (*1913*): the phase difference between two opposite electromagnetic coherent light-waves (clockwise: *cw*, resp. counter-clockwise: *ccw*), propagating in a rotating closed optical path, is proportional to the rotation rate (see the interferometer principle in Fig. 8).
The Sagnac formula:

$$\Delta\varphi_S = \frac{8\pi A}{c_0 \lambda_0} \cdot \Omega \tag{2.2-1}$$

shows the dependence of the phase deviations $\Delta\varphi_S$ from the angular rate Ω with a direct proportionality A (the interferometer's area, with an arbitrary form); the other factors are c_0, the vacuum light velocity, and λ_0, the wavelength of the lasing light. For a non-circular perimeter, one uses the vectorial form to derive the Sagnac formula, resulting in a similar expression *[Rodloff, 1999]*.

2.2.1. Dithered Ring Laser Gyroscope

According to Maxwell's laws for electrodynamic media, a standing-wave, which remains stable in the inertial frame, develops in the closed cavity of a Ring Laser Gyroscope.

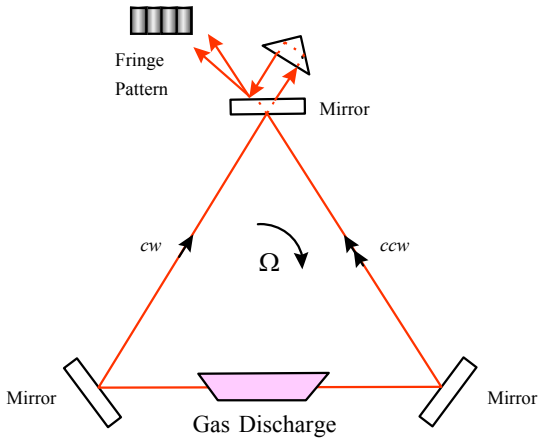

Fig. 9 *Ring Laser Gyroscope – simplified diagram [Savage, 1984]*

The Honeywell RLG type GG1320 – typical gyroscope sensor for strapdown navigation systems of the 1 nmi/h class – is realized in the form of a triangular resonant cavity of total length L (see the principle diagram in Fig. 9) with an active component (He-Ne Laser) that compensates the propagation losses. The two interfering light fascicles make an angle of some tens of arcsecond.

For the resonant cavities with a fundamental monomodal propagation of TEM (Transversal Electro-Magnetic) waves, the length of the optical path needs to be an integer multiple of the wavelength:

$$m \cdot \lambda_{\pm} = L_{\pm}\,, \qquad (2.2\text{-}2)$$

where $\lambda_{\pm}$ represent the wavelength of the *cw*, resp. *ccw* propagating waves, $L_{\pm}$ are the *cw*, resp. *ccw* light paths and m is an integer number. Through differentiation, considering small variations and using the relation $\lambda = c_0 / f$, one obtains for the non-rotating case *[Killpatrick, 1967]*:

$$\left|\frac{\Delta f}{f}\right| = \left|\frac{\Delta L}{L}\right|. \qquad (2.2\text{-}3)$$

With the Sagnac-interferometer relation: $\Delta L = c_0 \cdot \Delta\tau_s$, we find the dependence of the difference Δf (between the frequencies of the two opposite propagating spatial light-waves *cw*, resp. *ccw*) from the angular rate Ω:

$$\Delta f = \frac{4A}{\lambda L} \cdot \Omega\,. \qquad (2.2\text{-}4)$$

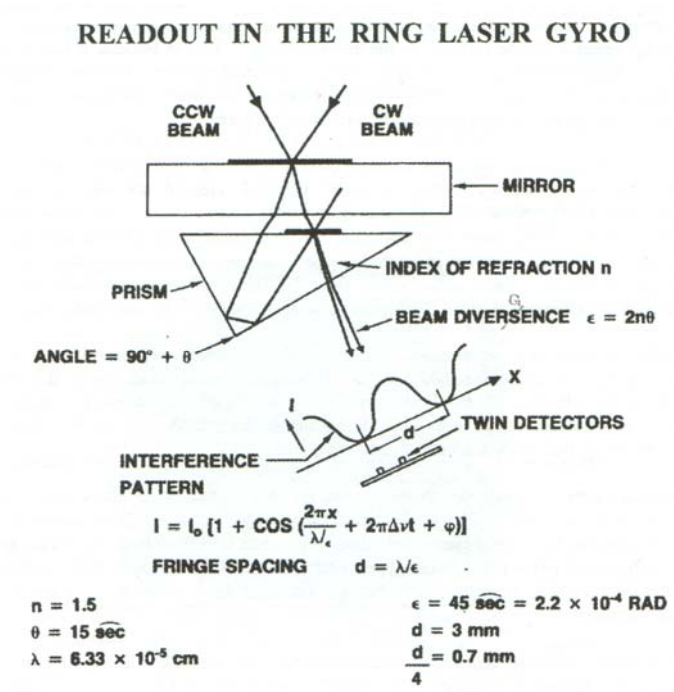

Fig. 10 *Early readout technique used by Ring-Laser Gyroscopes [from Aronowitz,1999]*

Fig. 10 presents in a suggestive manner the early readout technique used by RLG. Considering the convergence angle ε of the propagation directions of the two interfering plane waves and assuming their amplitude equality ($E_+ = E_- = E$), the complex form of their superposition is:

$$\underline{E}_t = E \cdot [e^{j(2\pi f \cdot t - \mathbf{k}_1 \cdot \mathbf{r} + \varphi_{01})} + e^{j(2\pi(f+\Delta f)\cdot t - \mathbf{k}_2 \cdot \mathbf{r} + \varphi_{02})}]\,, \qquad (2.2\text{-}5)$$

with:

$$\frac{(\mathbf{k}_2 - \mathbf{k}_1)\cdot \mathbf{r}}{2} = \frac{2\pi}{\lambda} \cdot \sin(\frac{\varepsilon}{2}) \cdot x \quad \text{and}$$

$$\frac{(\mathbf{k}_2 + \mathbf{k}_1)\cdot \mathbf{r}}{2} = \frac{2\pi}{\lambda} \cdot \cos(\frac{\varepsilon}{2}) \cdot y\,,$$

where x and y are the transversal resp. the longitudinal axes. The light intensity of the interference pattern in the transversal plane (orthogonal to the bisecting line of the convergence angle), proportional to the temporal mean of the squared electric field intensity *[Pedrotti, 2003]*, can be put in the form (also by taking into account the small value of the convergence angle ε):

$$I = \frac{E^2}{Z_0} \overline{\cos^2(2\pi \frac{\Delta f}{2} t - \frac{2\pi}{\lambda/\varepsilon} x + \varphi_0^-) \cdot \sin^2(2\pi(f + \frac{\Delta f}{2})t - \frac{2\pi}{\lambda} x + \varphi_0^+)}\,, \qquad (2.2\text{-}6)$$

where I is expressed in [W/m²], $Z_0 = 377\ \Omega$ (the vacuum wave impedance) and E is given in [V/m] (the overscore denotes averaging).

After some algebraic manipulations, considering only the expression of the light intensity on a transversal screen (phase dependencies along the space variable x), one obtains the relation:

$$I_{transv} = I_0 \cdot [1 + \cos(\frac{2\pi}{\lambda / \varepsilon} x + 2\pi \Delta f \cdot t + \varphi_0)] \,. \qquad (2.2\text{-}7)$$

In the absence of a gyroscope rotation ($\Delta f = 0$ for $\Omega = 0$), one gets a stationary fringe model (with a sinusoidal light intensity variation), with distances d between the successive intensity maxima inverse proportional to the convergence angle ε: $d = \lambda / \varepsilon$ (corresponding to phase shifts of 2π along the transversal axis x). In the presence of finite rate values, the second term of the cosine function argument (eq. 2.2-7), a time phase variation, implies a displacement of the fringe model in the direction determined from the sign of the frequency difference Δf (between the two opposite Laser light-waves). The interference fringes (100 % modulation) are moving in the detector window with a velocity proportional to the gyroscope angular rate Ω (see Fig. 10), the number of the fringes in a given time being proportional to the rotation angle. Providing two light intensity detectors, one can quantify both the rotation amplitude (through counting the number of succeeding fringes per unity of time interval), as well as the rotation sense (through the quadrature-mounting of detectors in respect to the fringe pattern).

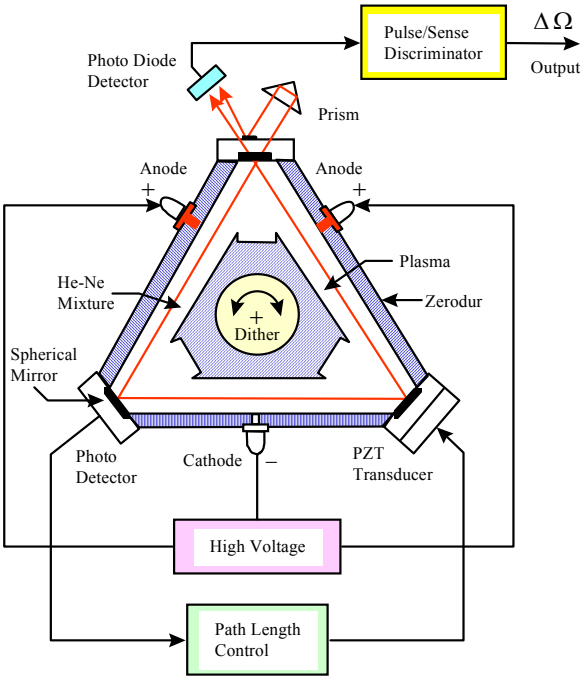

Fig. 11 *Principle of an active laser gyroscope [Savage, 1984-a]*

In Fig. 11 a typical physical realization of a RLG is presented. The plasma-cavity (equilateral triangular form) is milled in a thermo-stable dielectric material – Cervit or Zerodur (thermal dilatation coefficient: $5 \cdot 10^{-9}$ [1/K]). One can see also the piezoelectric ceramic transducer (*PZT*) for the control-loop of the resonant cavity optical length, mounted on a reflecting mirror. The voltage furnished by the high voltage generator (typically 1500 V), that produces the ionization of the He-Ne gas mixture, is applied to a pair of symmetric anodes (to compensate the plasma leakage – Langmuir effect, that could create an asymmetrical modification of the refraction index of the resonant cavity in the case of non-compensation). One can see also the dither-mechanism, used to compensate the lock-in effect (no signal output in the vicinity of zero rates), the pick-off optic and the signal detection (delivering the number of pulses per second, proportional to the rotation rate, and the rotation sense information).

The triangular form of the RLG, with the drawback of a poorer sensitivity and of greater reflection angles (enhancing the lock-in effect) in comparison with the quadratic form, has the advantage of saving one reflecting surface. An important life limitation is given through the continuous contamination due to diffusion into the Laser cavity: one eliminates partially this effect by providing activated "getter" in some cavity-niches. The principal life limitation of the RLG is caused through the "cleanup" of the gas mixture: by operating the Laser, the Neon atoms are gradually imbedded in the cathode, through the ionizing gas discharge.

Contemporary techniques permit to obtain a count output for essential less than a full fringe motion: factors of 1000 were reported, that means a count for about 0.01 arcsec.
The scale factor, defined as the rotation angle corresponding to a single fringe (i = 1), is expressed as:

$$\alpha_{i=1} = \frac{\lambda L}{4A} \text{ [rad/pulse]} \qquad (2.2\text{-}8)$$

A numerical example for an usual triangular RLG with a side length of 20 cm, having a wavelength of the He-Ne Laser radiation of 632.8 nm and with the scale factor expressed in [arcsec/pulse], gives:

$$\alpha_{i=1} = \frac{632.8 \cdot 10^{-9} \cdot 3 \cdot 0{,}2}{4 \cdot 0.2 \cdot 0.2 \cdot \frac{\sqrt{3}}{2} \cdot \frac{1}{2}} \cdot \frac{648000}{\pi} \cong 1.13 \text{ arcsec/pulse.}$$

This value represents also the resolution in the angle determination, when no enhanced detection techniques are used.

The essential drawback of the Ring Laser Gyroscope (RLG) is the „lock-in“ effect: The transfer function (frequency deviation / angular rate) is not linear: for reduced angular velocities around the null value, the frequency deviations are also null (see Fig. 12).
The analytical expression of that function (without physical significance) is:

$$\Delta f = \begin{cases} 0, & |\Omega| < \Omega_{L\_I} \\ \frac{4A}{\lambda L} \cdot \sqrt{\Omega^2 - \Omega_{L\_I}^2}, & |\Omega| \geq \Omega_{L\_I} \end{cases} \qquad (2.2\text{-}9)$$

where: Ω_{L_I} = the dead zone delimiting rate (**L**ock-**I**n).

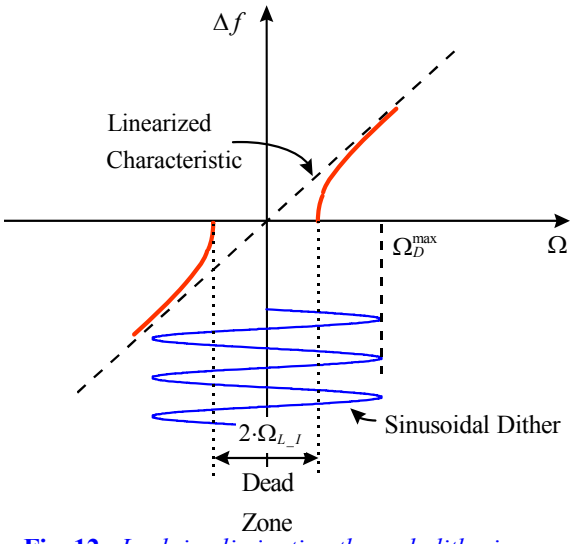

Fig. 12 *Lock-in elimination through dithering*

The lock-in occurs as a consequence of the coupling of the two *cw* and *ccw* waves – with closely oscillation frequencies – inside the resonant cavity. The coupling is principally due to the back-scattering on the mirror levels by the reciprocal energy injection from one wave to the other; this phenomenon is not present at greater frequency differences, which corresponds to greater input rates. Therefore the mirror quality is a key-factor for the realization of a valuable RLG.
An analytical expression of the limiting „lock-in“ rate Ω_{L_I} as a function of the constructive parameters of the RLG is *[Rodloff, 1994]*:

$$\Omega_{L\_I} = \frac{c_0 \lambda_0^2 \sqrt{r}}{32\pi A d}, \qquad (2.2\text{-}10)$$

with:
r = mirror‘s back-scattering coefficient
d = Laser’s plasma diameter (for a circular interferometer)
One can see that, by increasing the active RLG surface or equivalently, the plasma diameter, the boundary angular rate is diminished. Typical values are:

$\Omega_{L\_I} \approx 0.1$ deg/s $= 360$ deg/h

In the field of strapdown inertial navigation a broad domain of rotation rates is necessary: $\Omega \in$ (0,01 deg/h ...400 deg/s), therefore it is essential to eliminate the dead zone.
In principle there are two main ways to slide the operating point out from the dead zone:

- application of symmetrical gyroscope rotations, about the null position
- the use of Faraday and/or Kerr effects, to non-reciprocally modify the cavity refraction index by applying magnetic or electric fields to the transducers placed on the optical paths of the RLG.

Although the second method is more elegant, no mechanical movements are needed, in practice one uses still almost exclusively the symmetric mechanical oscillation rate (dither), usually generated by a sinusoidal electrical control (Fig. 12) of a piezoelectric ceramic block upon a stiff dither flexure suspension. The dither frequencies of the SIMU gyroscopes triad are chosen slightly different, in order to minimize the mechanic correlations inside the sensor block.
Assuming angular amplitude α_D of the sinusoidal dithering oscillation $\alpha(t)$ with the angular frequency ω_D and

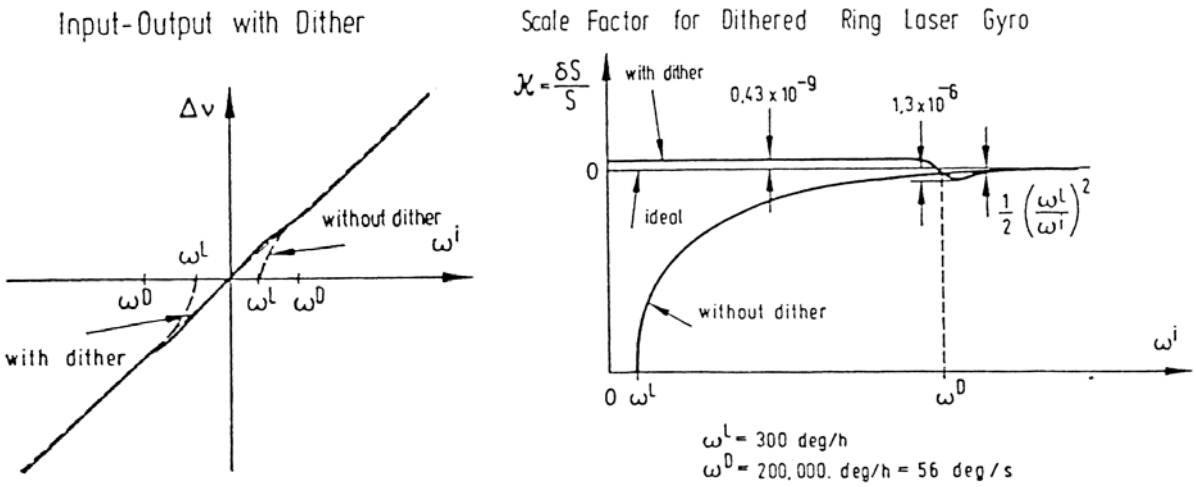

Fig. 13 *The actual lock-in effect manifestation, from [Stieler, 1995]*

without initial phase, the dither angular velocity is:

$$\Omega_D = \dot{\alpha}(t)$$
$$= \alpha_D \omega_D \cos(\omega_D \cdot t)\,.$$

The amplitude of the angular velocity Ω_D^{max}, using some typical values of the dithering system, is:

$$\Omega_D^{max} = 200 \cdot \frac{\pi}{180 \cdot 3600} \cdot 2 \cdot \pi \cdot 500 \cong 3.086 \text{ rad/s}$$
$$\cong 176.8 \text{ deg/s}\,,$$

with:

$$\alpha_D = 200 \text{ arcsec}$$
$$f_D = 500 \text{ Hz.}$$

Due to the existence of the relation $\Omega_D^{max} >> \Omega_{L\_I}$ (for the chosen realistic example), the dwell time Δt in the lock-in zone (for which the rotation rate is smaller then the limit rate of the dead zone: $|\Omega| < \Omega_{L\_I}$) is very small. However, there remains a little residual effect, through the input averaging for the dead zone interval, which causes a small residual amount of lock-in (affecting the linearity of the scale factor – see Fig. 13) and also a multiple steady-state lock-in.

The mechanical dither signal is usually eliminated from the gyroscope output signal by a proportional subtraction of the interference fringe pattern displacement from the dither rate fringe displacement sensed by the detector, through an adequate mounting of the output beam guiding prism on the mobile case of the gyroscope, and of the detector's photodiodes set on the firmly-mounted block.

By adding amplitude white noise to the sinusoidal dithering, which is equivalent to a phase noise (jitters), one avoids the laser locking onto the steady-state solution, the lock-in threshold being reduced to zero, however with the drawback of introducing of supplementary angular noise on the gyroscope output (twice each dither-cycle, at each passage of the input through the dead-band). The dithering procedure introduces also some noise to accelerometer sensors, mounted on the same mechanical unit.

The angular random walk noise (*ARW*), for the case of the randomized sinusoidal dither, can be expressed *[Aronowitz, 1999]* as uncertainty in the angle measurement:

$$\delta ARW = \Omega_{L\_I} \cdot \sqrt{\frac{S_k}{2\pi\Omega_D}}\,, \tag{2.2-11}$$

with:

S_k = the gyro scale factor in [arcsec/count].

An essential smaller component of the RLG ARW noise, the quantum limit (at least 10…20 times smaller), is caused by spontaneously emitted photons, always present in Laser emission.

Considering the same numerical values as in the precedent numerical examples, the main component of the angular random noise can be estimated:

$$\delta ARW = 0.1 \cdot \sqrt{\frac{1.13/3600}{2 \cdot \pi \cdot 176.8}} \cong 5.3 \cdot 10^{-5} \text{ [deg/}\sqrt{\text{s}}\text{]}$$
$$\cong 0.003 \text{ [deg/}\sqrt{\text{h}}\text{]},$$

which represents a typical value required for the 1 nmi/h navigation grade IMUs.

In Tab. 3 are given the principal parameters of the used Honeywell RLG type GG1320, which is a typical gyroscope sensor for strapdown navigation systems of the 1nmi/h class.

Tab. 3 *Principal parameters of the Honeywell Ring Laser Gyroscope type GG1320*

Quantity	Value
Bias stability error	≤ 0.002 °/h
Random walk noise	≤ 0.0018 °/$\sqrt{\text{h}}$
Scale factor stability/nonlinearity	≤ 10 ppm
Input axes alignment error	$\leq \pm 1$ mrad
Magnetic environment sensitivity	0.002 (°/h)/gauss
Maximal angular rate	±500 °/s
Lifetime (MTBF - Mean Time Between Failures)	$< 5 \cdot 10^4$ h

2.3. Inertial sensor error models

The inertial sensors of acceleration and rotation exhibit a lot of similarities in their error models. Therefore a common systematic approach is justified.
Basically, the error model has to cover several effects, such as the mounting uncertainties (related to the impossibility to physically align the input (sensitive) axes of sensors with the orthogonal reference triads), environmental influences (temperature, air pressure, magnetic fields, etc.), input/output nonlinear behavior (due to aging, saturation, hysteresis effects or dead zones), quantization (inherent to any discrete signal acquisition) and numerical errors, stochastic errors, etc. Whereas the principal part of the inertial sensor measurement errors can be estimated and compensated beforehand through the sensor calibration, the residual errors, as well as the stochastic ones, must be compensated during the process of the navigation solution computation itself, through the use of some external aiding information. Otherwise the solution becomes useless due to time accumulation of navigation errors.

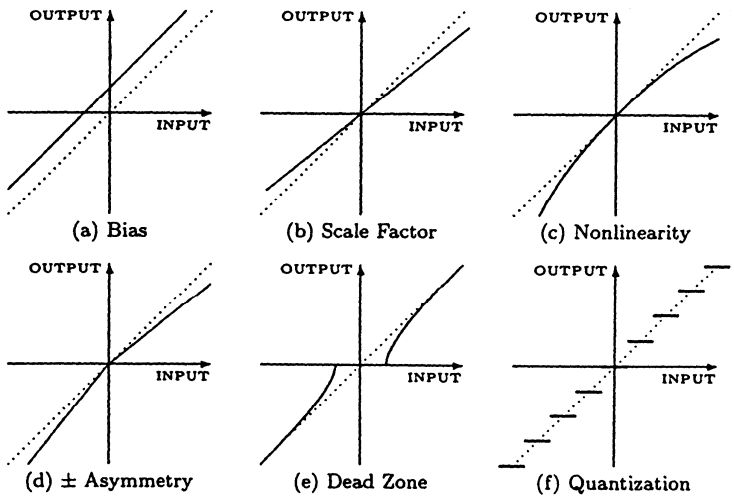

Fig. 14 *Common input/output error types, from [Grewal, 2001]*

Some of the common input/output sensor measurement error types are presented in Fig. 14.
A trade-off between the desired solution precision and the model complexity, by using of a great number of variables, must be made by designing an error estimation strategy. All error sources discussed in the following are the small, uncompensated ones, which are potential candidates for Kalman filtering estimation. It is assumed that the main part of these errors has been compensated through the preliminary data calibration. In Table 1 one can see the principal parts of errors for the used inertial sensors: the balanced accelerometers and ring laser gyroscopes.
Considering the two types of inertial sensors, referenced in their own axes system (quasi-orthogonal ones: accelerometer system x^a, y^a, z^a, resp. gyro system x^g, y^g, z^g, defined by the sensors input sensitive axes), one expresses the sensor inputs in the strapdown IMU reference system, denoted as the *body* reference system of the vehicle (in a simplified approach, we assume the coincidence between the vehicle *body* reference system and the SIMU-platform system, both originated in the vehicle's CoM (Centre of Mass)).

2.3.1. Accelerometer errors

We define the sensor input vector as containing the sensed quantities (accelerations in [m/s²]), respective the output vector containing the delivered sensor output values (e.g., accelerometer outputs in [V]). The measurement model for the accelerometer triad, expressed in error form *[Farell et al., 1999; Grewal et al., 2000; Rogers, 2000; Schwarz et al., 2001]*, in the *body* reference system (x^b, y^b, z^b), can be given as :

$$\mathbf{f}_{out}^b = (a\mathbf{SCF}^T \cdot \mathbf{I} + \delta a\mathbf{SCF} + \delta a\mathbf{MA}) \cdot \mathbf{f}_{in}^b + \delta\mathbf{b}_{acc} + \delta\mathbf{nl}_{acc} + \tilde{\mathbf{v}}_{acc} \qquad (2.3.1\text{-}1)$$

where the δ – symbol denotes a perturbation and the other symbols are explained as follows:

$$\mathbf{f}_{out}^b = \begin{bmatrix} f_{out_x}^b \\ f_{out_y}^b \\ f_{out_z}^b \end{bmatrix} \qquad (2.3.1\text{-}2)$$

is the vector of specific force measurement (accelerometer outputs, given, e.g., in [V]);

$$\mathbf{f}_{in}^b = \begin{bmatrix} f_{in_x}^b \\ f_{in_y}^b \\ f_{in_z}^b \end{bmatrix} \qquad (2.3.1\text{-}3)$$

is the vector of input specific force (sensed from accelerometers, given in [m/s²]);

$$a\mathbf{SCF} = \begin{bmatrix} aSCF_x \\ aSCF_y \\ aSCF_z \end{bmatrix}, \tag{2.3.1-4}$$

with $a\mathbf{SCF}$ denoting the constant part of the accelerometer scale factor vector;

$$\delta a\mathbf{SCF} = \delta a\mathbf{SCF}_{stability} + \delta a\mathbf{SCF}_{drift} + \delta a\mathbf{SCF}_{temp} = \tag{2.3.1-5}$$

$$\begin{bmatrix} \delta aSCF_{stability_x} + \delta aSCF_{drift_x} + \delta aSCF_{temp_x} & 0 & 0 \\ 0 & \delta aSCF_{stability_y} + \delta aSCF_{drift_y} + \delta aSCF_{temp_y} & 0 \\ 0 & 0 & \delta aSCF_{stability_z} + \delta aSCF_{drift_z} + \delta aSCF_{temp_z} \end{bmatrix}$$

is the diagonal matrix of uncompensated accelerometer scale factor errors, expanded as a sum of an uncompensated **offset** term, the turn-on to turn-on offset $\delta aSCF_{stability}$, of the time-dependent **drift** function $\delta aSCF_{drift} = f_{drift}(t)$ and of the **temperature** dependent error term:

$$\delta a\mathbf{SCF}_{temp} = \delta a\mathbf{SCF}_{temp\ cal} + \delta a\mathbf{SCF}_{temp\ res}\,. \tag{2.3.1-6}$$

The principal part of the scale factor temperature dependencies $\delta a\mathbf{SCF}_{temp\ cal}$ is habitually eliminated in the step of IMU's preliminary sensor-data processing and is modelled, for each accelerometer, through a four-degree polynomial error expression *[AlliedSignal, 1998]:*

$$\delta aSCF_{temp\ cal} = \sum_{k=1}^{k=4} \delta aSCFK_{temp\ cal_k} \cdot (T - T_{cal})^k\,, \tag{2.3.1-7}$$

where $\delta aSCFK_{temp\ cal_k}$ are constant coefficients and the quantity $T - T_{cal}$ represents the temperature difference between the actual accelerometer temperature and the reference temperature by calibration.
The uncompensated residual part of the scale factor temperature dependency is modelled for each accelerometer also as a polynomial dependence, of order *n* in temperature variation and can be estimated through modelling of the polynomial coefficients $\delta aSCFK_{temp\ res_i}$ as random constant variables in a Kalman filter implementation:

$$\delta aSCF_{temp\ res} = \sum_{i=1}^{i=n} \delta aSCFK_{temp\ res_i} \cdot (T - T_{cal})^i\,.$$

Of course, the above expressions must be considered for all three (*x*, *y*, *z)* accelerometers. For more precise sensor error models one accounts not only for the temperature changes from the nominal value, but also for the temperature gradients ∇T ,respectively for magnetic field influences (see below the similar model description for the bias errors). The residual parts of the uncompensated accelerometer scale factor errors are usually in the range of ≤ 70 ppm;

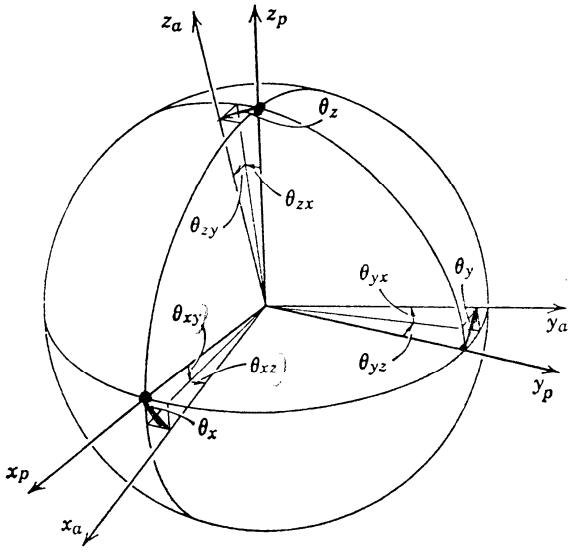

Fig. 15 *Link between the **a**ccelerometer reference system and the measuring **p**latform system, from [Britting, 1971]*

The term:

$$\delta a\mathbf{MA} = \begin{bmatrix} 0 & \delta aMA_{xy} & \delta aMA_{xz} \\ \delta aMA_{yx} & 0 & \delta aMA_{yz} \\ \delta aMA_{zx} & \delta aMA_{zy} & 0 \end{bmatrix} \tag{2.3.1-8}$$

is an off-diagonal matrix which accounts for the misalignments between the accelerometer reference system (materialized by the accelerometer triad input axes) and the SIMU reference frame (orthogonal triad). All these coefficients are temperature dependent and must be compensated in the same manner as the accelerometer scale factors and biases, through fourth-order polynomials:

$$\delta aMA = \sum_{k=1}^{k=4} \delta aMA_{temp\ cal_k} \cdot (T - T_{cal})^k\,. \tag{2.3.1-9}$$

The link between the accelerometer reference system and the measuring platform system (in our case the strapdown IMU *body* system) is presented in Fig. 15.

These errors are of the order of $2.5 \cdot 10^{-7}$ rad. A more complex model can use supplementary dependencies from

the temperature gradients ∇T and from the magnetic field influences, as usually applied by scale-factor and bias error modelling;
The expression:

$$\delta\mathbf{b}_{acc} = \begin{bmatrix} \delta aB_{0x} + \delta aRC_x + \delta aBRD_x + \delta aBED_x + \delta aCF_x \\ \delta aB_{0y} + \delta aRC_y + \delta aBRD_y + \delta aBED_y + \delta aCF_y \\ \delta aB_{0z} + \delta aRC_z + \delta aBRD_z + \delta aBED_z + \delta aCF_z \end{bmatrix} \quad (2.3.1\text{-}10)$$

represents the vector of biases, defined as the sum of all perturbations that are resulting by zero inputs ($\mathbf{f}_{in}^{b} = \mathbf{0}$) in relation (2.3.1-1), excepting the white noise and the nonlinearity errors (the residual bias is of the order of 25 μg). By Kalman filtering implementation each random constant or drift term is modelled through a differential equation, in accordance to the individual stochastic noise process. The terms in the above relation are:

δaB_0 = a **constant acceleration offset**, whose principal part is already eliminated through the SIMU calibration (laboratory calibration and coarse/fine alignment);

δaRC = the turn-on to turn-on offset (called also **bias stability**), modelled as a random constant: $\dot{\delta} aRC = 0$; it can be caused, e.g., by the thermal cycling of inertial sensors (their mechanical components and electronics);

$\delta aBRD$ = a **bias drift of random nature**, that is the bias variability after the turn-on caused from accelerometer mechanical and electronic components stochastic parameter modifications (such as ageing processes of the stiffness, contribution of the electronic noises, etc.). It has more additive components; the principal ones are detailed below (for more details see also *[IEEE Std. 647-1995]*):

$$\delta aBRD = \delta aVelRW + \delta aGM + \delta aQ + \delta aBI + \delta aAccRW + \ldots, \quad (2.3.1\text{-}11)$$

where:

$\delta aVelRW$ = accelerometer **drift** modelled as a stochastic **Random Walk** process (typical values of the RW noise for our QA2000-40 accelerometer: 8μg/sqrt(Hz)); the process differential equation is:

$$\dot{\delta} aVelRW = wn, \quad (2.3.1\text{-}12)$$

with $wn \sim (N, 0)$, stochastic Gaussian white noise process of amplitude N and zero mean value;

δaGM = time-correlated acceleration **drift**, modelled as a **Gauss-Markov first order** stochastic noise process *[Rogers, 2000]*, characterized through the differential equation:

$$\dot{\delta} aGM = -\beta \cdot \delta aGM + \sqrt{2\beta\sigma^2_{\delta aGM}}, \quad (2.3.1\text{-}13)$$

with β the inverse of the correlation time;

δaQ = **quantization error**, with an assumed uniform statistic distribution in the interval ($-LSB/2 \ldots +LSB/2$) (LSB is the Least Significant Bit value of the A/D converter); its variance is $\sigma^2_{aQ} = LSB^2/12$. Considering the resolution of the 24-Bit A/D converter by measuring with the Full Scale acceleration domain of 2g ($FS_{acc} = 2g \approx 19.82$ m/s²) as being $LSB = FS_{acc}/2^{24-1}$ (one Bit is used for the sign information), the standard deviation of the quantization error results about 0.068 μg;

δaBI = **drift** of **low-frequency** nature (called also **bias instability** *[IEEE Std. 647-1995]*); this 1/f random process has a –1 slope in a log-log PSD (Power Spectrum Density) representation and is manifested as a bias fluctuation;

$\delta aAccRW$ = a **very low-frequency** random **drift**, with a 1/f² variation in the PSD diagram (slope of –2 in the log-log representation)

$\delta aBED$ = residual **bias drift** caused by random **environmental** parameters variations (e.g., temperature, external magnetic fields, etc.);
As usually, more precise models account not only for the temperature changes from nominal, ΔT, but also for temperature gradients ∇T and also for magnetic field influences (here is considered the vector of **m**agnetic induction ***B***):

$$\delta aBED = \delta aB\Delta T + \delta aB\nabla T + \delta aBM + \ldots \quad (2.3.1\text{-}14)$$

By existing of supplementary data regarding environmental parameter variations, one can eliminate, through a careful calibration, the most significant part of this errors. For example, the main bias temperature compensation – made similar for the accelerometer scale factor – uses the same intern-mounted temperature sensors and also a four-degree polynomial dependency in the form: $\delta aB\Delta T = \delta aBK_T \cdot f(T - T_{cal})$, where δaBK_T is the coefficient of the bias/temperature dependency (of the order of 5 μg/°C) and $f(T - T_{cal})$ represents a polynomial function of the temperature changes from nominal;

δaCF = a weak acceleration error (of centrifugal nature), caused by the offset between the origin of the accelerometer-system reference point and the effective centre of accelerometer (physically, not all accelerometers can be positioned simultaneously on the same point, the origin of the accelerometer triad). For the *i*-th accelerometer, the magnitude of this error is then: $\delta aCF = \omega_{\perp}^2 \cdot r_i$, with $\omega_{\perp}$ the rate about an axis perpendicular to the position vector $\mathbf{r}_i$ of the accelerometer centre. Under strapdown navigation conditions this error could become important, especially in the case of extreme rates, in the range of ±500 [deg/s] (a 1 mm offset causes already an error of about 0.076 m/s²);

$$\delta\mathbf{nl}_{acc} = \begin{bmatrix} \delta aK_{x_{xx}} & \delta aK_{x_{yy}} & \delta aK_{x_{zz}} & \delta aK_{x_{xy}} & \delta aK_{x_{yz}} & \delta aK_{x_{zx}} \\ \delta aK_{y_{xx}} & \delta aK_{y_{yy}} & \delta aK_{y_{zz}} & \delta aK_{y_{xy}} & \delta aK_{y_{yz}} & \delta aK_{y_{zx}} \\ \delta aK_{z_{xx}} & \delta aK_{z_{yy}} & \delta aK_{z_{zz}} & \delta aK_{z_{xy}} & \delta aK_{z_{yz}} & \delta aK_{z_{zx}} \end{bmatrix} \cdot \begin{bmatrix} (\mathrm{f}_{in_x}^b)^2 \\ (\mathrm{f}_{in_y}^b)^2 \\ (\mathrm{f}_{in_z}^b)^2 \\ \mathrm{f}_{in_x}^b \cdot \mathrm{f}_{in_y}^b \\ \mathrm{f}_{in_y}^b \cdot \mathrm{f}_{in_z}^b \\ \mathrm{f}_{in_z}^b \cdot \mathrm{f}_{in_x}^b \end{bmatrix} \tag{2.3.1-15}$$

is the matrix of **accelerometer nonlinearities**, caused by second order nonlinearity errors (dependent on the quadratic terms of the *body* input specific force components) and also by cross-coupling accelerometer errors (dependent on the product terms of the *body* input specific force components). These coefficients can be estimated in a Kalman filter implementation, being modelled as random constant coefficients;
The term:

$$\tilde{\mathbf{v}}_{acc} = \begin{bmatrix} aWN_x \\ aWN_y \\ aWN_z \end{bmatrix} \tag{2.3.1-16}$$

is the vector of the white noise present in the accelerometer data, caused by the electronics and by the multitude of residual unmodelled stochastic processes (like the finite precision effects, etc.) that together (in accordance to the central statistics theorem) have the properties of additive white noise.

If the error dependence (relation 2.3.1-1) is invertible, one can explicitly express the input quantities in this relation, deriving a "compensation form" of the error model *[Grewal et al., 2000]*, which can be used directly by the navigation solution implementation:

$$\mathbf{f}_{in}^b = (a\mathbf{SCF}^T \cdot \mathbf{I} + \delta a\mathbf{SCF} + \delta a\mathbf{MA})^{-1} \cdot (\mathbf{f}_{out}^b - \delta\mathbf{b}_{acc} - \delta\mathbf{nl}_{acc} - \tilde{\mathbf{v}}_{acc}) . \tag{2.3.1-17}$$

2.3.2. Gyroscope errors

Similar to the accelerometer error definition, again considering the input vector as being formed from the sensed quantities (angular rates in [deg/s]) and the output vector formed from the sensor outputs (e.g., gyro outputs in [pulse/s]), the measurement model of the gyroscopes triad, expressed in the error form *[Farell et al., 1999; Grewal et al., 2000; Rogers, 2000; Schwarz et al., 2001]* in the *body* reference system can be given as:

$$\boldsymbol{\omega}_{out}^b = (g\mathbf{SCF}^T \cdot \mathbf{I} + \delta g\mathbf{SCF} + \delta g\mathbf{MA}) \cdot \boldsymbol{\omega}_{in}^b + \delta\mathbf{b}_{gyro} + \delta\mathbf{nl}_{gyro} + \delta g\mathbf{k}_{acc} + \tilde{\mathbf{v}}_{gyro} , \tag{2.3.2-1}$$

where the symbols have, corresponding to the *gyro* sensors, similar significations as above (up to *g*-notations in the relation 2.3.1-1); the additional term $\delta g\mathbf{k}_{acc}$ states explicitly the small acceleration-dependent errors.
In opposite to the acceleration sensors, the used Ring Laser Gyroscopes present negligible temperature dependent errors (of about 0.00005 (deg/h)/°C); also the acceleration dependent errors are very small, situated in the range of 0.0002 (deg/h)/g, as well as the gyro scale factor asymmetry, of about 1 ppm, which is also negligible for

navigation-grade IMUs. The residual error dependency on the earth magnetic field is minimized in our case through the use of an appropriate magnetic shielding, provided for the whole sensor block.
In the expanded form, the error model has the following components (observe the similarities with the accelerometer error model):

- Residual scale factor errors:

$$\delta g\mathbf{SCF} = \delta g\mathbf{SCF}_{stability} + \delta g\mathbf{SCF}_{drift} + \delta g\mathbf{SCF}_{temp} = \tag{2.3.2-2}$$

$$\begin{bmatrix} \delta gSCF_{stability_x} + \delta gSCF_{drift_x} + \delta gSCF_{temp_x} & 0 & 0 \\ 0 & \delta gSCF_{stability_y} + \delta gSCF_{drift_y} + \delta gSCF_{temp_y} & 0 \\ 0 & 0 & \delta gSCF_{stability_z} + \delta gSCF_{drift_z} + \delta gSCF_{temp_z} \end{bmatrix}$$

One observe that no gyro thermal compensation is introduced – the temperature errors in the case of the Ring Laser Gyroscopes are very small, as they use optical-way length compensation; only small residuals of temperature-dependent scale factor errors and bias errors are usually modelled in view of estimation in a Kalman filtering implementation.

- Gyroscopes axes misalignment:

$$\delta g\mathbf{MA} = \begin{bmatrix} 0 & \delta gMA_{xy} & \delta gMA_{xz} \\ \delta gMA_{yx} & 0 & \delta gMA_{yz} \\ \delta gMA_{zx} & \delta gMA_{zy} & 0 \end{bmatrix}, \text{ with typical values of } \le 10^{-3} \text{ rad for our gyroscopes} \tag{2.3.2-3}$$

- Residual biases:

$$\delta\mathbf{b}_{gyro} = \begin{bmatrix} \delta gB_{0x} + \delta gRC_x + \delta gBRD_x + \delta gBED_x \\ \delta gB_{0y} + \delta gRC_y + \delta gBRD_y + \delta gBED_y \\ \delta gB_{0z} + \delta gRC_z + \delta gBRD_z + \delta gBED_z \end{bmatrix}. \tag{2.3.2-4}$$

In the literature the gyro biases are denoted sometimes as drifts, referring to the associated angle time-variation (drift) by constant rate biases. The term δgB_0 represents the constant rate offset and δgRC is the turn-on to turn-on random offset. In Tab. 3 one sees the typical values of bias stability ($\delta gRC \le 0.002$ deg/h). The other two terms in (2.3.2-4) are explained as follows. The term:

$$\delta gBRD = \delta gARW + \delta gGM + \delta gQ + \delta gBI + \delta gRRW + ... \tag{2.3.2-5}$$

represents the random drift of the rate bias. The principal part of the bias random drift consists of the Angular Random Walk term $\delta gARW$ (with $\sigma_{ARW} \le 0.0018 \text{ deg}/\sqrt{\text{h}}$, see Tab. 2). Other components are the Gauss-Markov first-order stochastic process term δgGM , the low-frequency nature gyro Bias Instability δgBI and the Rate Random Walk $\delta gRRW$. For the rate quantization noise term δgQ the standard deviation can be estimated assuming a RLG angular-resolution of 1.113 arcsec/pulse (calibration value for our GG1320 gyros; see also section 2.2.1), to approx. $9 \cdot 10^{-5}$ deg/s, i.e. $2.5 \cdot 10^{-8}$ deg/h.
The error terms of the environmental-dependent bias drift:

$$\delta gBED = \delta gBM + \delta gT + ... \tag{2.3.2-6}$$

account for the dependence of the measured rotation rate on the magnetic field variations (considered is the **m**agnetic induction vector ***B***), through interactions with the gyroscope Laser plasma, as well as for the temperature dependency. For our navigation-grade RLG the magnetic bias is in the order of 0.002 (deg/h)/gauss (the earth magnetic induction magnitude has a variation of about 0.3…0.69 gauss between the magnetic equator and magnetic North Pole). Also the temperature-induced biases δgT for the ring laser gyroscopes are very low (about 0.00005 (deg/h)/°C) due to the continuous path-length control of the laser gyroscopes.

- Residual nonlinearities $\delta\mathbf{nl}_{gyro}$:

The uncompensated nonlinearity error terms are made very small by using the dithering technique; the acceleration-dependent errors (eventually induced by dithering oscillatory movement) of the Ring Laser Gyroscopes are also

negligible. That simplifies the error model. The gyro scale factor asymmetry of 1 ppm is also negligible for navigation-grade IMUs.

- Acceleration-sensitive errors

$$\delta g\mathbf{k}_{acc} = \begin{bmatrix} \delta gK_{x_x} & \delta gK_{x_y} & \delta gK_{x_z} & \delta gK_{x_{xx}} & \delta gK_{x_{yy}} & \delta gK_{x_{zz}} & \delta gK_{x_{xy}} & \delta gK_{x_{yz}} & \delta gK_{x_{zx}} \\ \delta gK_{y_x} & \delta gK_{y_y} & \delta gK_{y_z} & \delta gK_{y_{xx}} & \delta gK_{y_{yy}} & \delta gK_{y_{zz}} & \delta gK_{y_{xy}} & \delta gK_{y_{yz}} & \delta gK_{y_{zx}} \\ \delta gK_{z_x} & \delta gK_{z_y} & \delta gK_{z_z} & \delta gK_{z_{xx}} & \delta gK_{z_{yy}} & \delta gK_{z_{zz}} & \delta gK_{z_{xy}} & \delta gK_{z_{yz}} & \delta gK_{z_{zx}} \end{bmatrix} \cdot \begin{bmatrix} \mathrm{f}^b_{in_x} \\ \mathrm{f}^b_{in_y} \\ \mathrm{f}^b_{in_z} \\ (\mathrm{f}^b_{in_x})^2 \\ (\mathrm{f}^b_{in_y})^2 \\ (\mathrm{f}^b_{in_z})^2 \\ \mathrm{f}^b_{in_x} \cdot \mathrm{f}^b_{in_y} \\ \mathrm{f}^b_{in_y} \cdot \mathrm{f}^b_{in_z} \\ \mathrm{f}^b_{in_z} \cdot \mathrm{f}^b_{in_x} \end{bmatrix} \qquad (2.3.2\text{-}7)$$

Although this type of error is negligible for the Ring Laser Gyroscopes; the first and second order acceleration-sensitive errors have been explicitly expressed, with corresponding gyroscope coefficients δgK in a matrix-dependency form, as well as with the appropriate terms of *body*-system specific force input vectors. These coefficients could be estimated, in the usual manner, by modelling them as random constants in a Kalman filtering implementation. Usually values for the gyro g-sensitive biases, by navigation-grade IMUs, are in the range of 0.0002 (deg/h)/g.

- Finally, white noise terms (Gaussian, with zero mean):

$$\tilde{\mathbf{v}}_{gyro} = \begin{bmatrix} gWN_x \\ gWN_y \\ gWN_z \end{bmatrix}. \qquad (2.3.2\text{-}8)$$

The corresponding "compensation form" of the gyroscopes measurement model is (see relation 2.3.2-1):

$$\boldsymbol{\omega}^b_{in} = (g\mathbf{SCF}^T \cdot \mathbf{I} + \delta g\mathbf{SCF} + \delta g\mathbf{MA})^{-1} \cdot (\boldsymbol{\omega}^b_{out} - \delta\mathbf{b}_{gyro} - \delta\mathbf{nl}_{gyro} - \delta g\mathbf{k}_{acc} - \tilde{\mathbf{v}}_{gyro}) \qquad (2.3.2\text{-}9)$$

This quite detailed inventory of sensor errors shows that the use of such large Kalman vectors, as mentioned in the literature, seems to be reasonable (see for example Hua *[Hua, 2000],* who uses 144 parameter for the estimation of the model error coefficients in the GPS/INS integration).
In the presence of vibrations, induced by dithering, vehicle motor oscillations, particular movements of the vehicle, or by disregarding the variation of the sensed rotation rates between two successive sampled discrete values, some additional errors are induced. Examples are sculling acceleration errors (induced, e.g., on the vertical third-axis, associated with navigation along a sinusoidal horizontal trajectory, which implies phase correlated horizontal translations and yaw rotations) or coning errors (associated with phase-correlated oscillatory movements about two input axes, with the effect of a rotation error in the third axis – an apparent movement on a conic surface). Using high-rate pre-processing algorithms, with a sufficient number of terms *[Bose, 2000],* one can maintain the errors of the algorithm significantly below the values of the sensor errors (e.g., smaller than the bias stabilities of the accelerometers and gyros). The effects of assuming the rates to be constant between two successive samplings could be essentially minimized by employing very high data acquisition rates, which is often impractical.

3. Strapdown navigation mechanization and post processing results

3.1. Strapdown mechanization

The actual IMU strapdown mechanization (the processing of the navigation solution) is made in the rotating ECEF (Earth Centered Earth Fixed) reference system (*e*-frame), where the acceleration integration takes place; the navigation parameter values are expressed in the ENU (East, North, Up, with Up-axis orthogonal to the reference ellipsoid) navigation reference system (*n*-frame), which also allows easy interpretation (see Fig. 16). Actually one cannot carry out the integration directly in the *n*-frame *[Jekeli, 2001]*, where, by definition, no horizontal movement occurs: the *n*-frame mechanisation is then formally derived by coordinatizing the velocity vector (determined, e.g., in the *e*-frame, where the effective vehicle movement takes place) in the local geodetic system ENU.

Taking into account the Coriolis accelerations, due to the movement on the rotating earth surface, the *e*-frame navigation state equations have the vectorial form *[Schwarz et al., 2001]*:

$$\begin{bmatrix} \dot{\mathbf{r}}^e \\ \dot{\mathbf{v}}^e \\ \dot{\mathbf{C}}_b^e \end{bmatrix} = \begin{bmatrix} \mathbf{v}^e \\ \mathbf{C}_b^e \mathbf{f}^b - 2\boldsymbol{\Omega}_{ie}^e \mathbf{v}^e + \mathbf{g}^e \\ \mathbf{C}_b^e (\boldsymbol{\Omega}_{ib}^b - \boldsymbol{\Omega}_{ie}^b) \end{bmatrix}, \tag{3.1-1}$$

with:

$\mathbf{r}^e$, $\mathbf{v}^e$: position and respectively velocity vectors in the *e*-frame

$\mathbf{C}_b^e$: transformation matrix from the *b*-frame to *e*-frame

$\mathbf{f}^b$: specific-force vector (accelerometer measurement)

$\boldsymbol{\Omega}_{ie}^e$: the skew-symmetric matrix of earth rotation rate $\boldsymbol{\omega}_{ie}$, expressed in the *e*-frame

$\mathbf{g}^e$: normal gravity in the conventional *e*-frame ($\boldsymbol{\gamma}^e$ vector *[Schwarz, 2001]*, orthogonal to the reference ellipsoid). The gravity disturbance: $\delta\mathbf{g}^e = \mathbf{g}^e - \boldsymbol{\gamma}^e$ is considered null in this model; it can be thought as included in the system noise-model

$\boldsymbol{\Omega}_{ib}^b$: the skew-symmetric matrix of *b*- to *i*-frame rotation (rate $\boldsymbol{\omega}_{ib}^b$), expressed in the *b*-frame

$\boldsymbol{\Omega}_{ie}^b$: the skew-symmetric matrix of *e*- to *i*-frame rotation (rate $\boldsymbol{\omega}_{ie}^b$), expressed in the *b*-frame

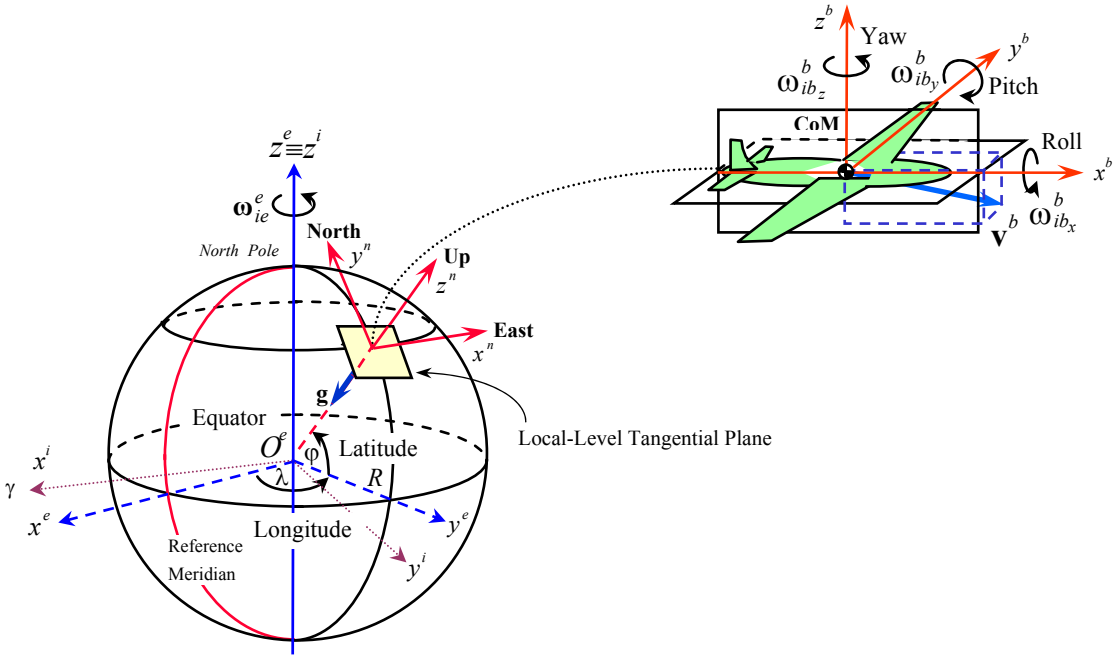

Fig. 16 *Relations between* ***operational inertial-****,* ***earth-****,* ***navigation-*** *and* ***body-frame***

Fig. 17 represents graphically the above mechanization in the earth-fixed *e*-frame (see Fig. 16 for relations between the reference frames). The mechanization is executed step-wise: first the integration of the rotation transformation matrix is carried out, and secondarily the transformation of the specific-force vector components from the *b*- to the *e*-frame. The algorithm is recursive: the rotation matrix $\mathbf{C}_b^e$ is needed before its integration, for the transformation of the rate vectors $\boldsymbol{\omega}_{ie}^b$, $\boldsymbol{\omega}_{ib}^b$ to the *e*-frame; also the determined velocities and positions (e.g., in curvilinear coordinates form) are needed before the velocity integration, in order to compensate the transformed specific-force measurement vector $\mathbf{f}^e$ for the Coriolis and the gravity accelerations.

The general form of error state equations used in the Kalman filtering (obtained by linearizing the INS mechanization equation system) has the form:

$$\delta\dot{\mathbf{x}} = \mathbf{F} \cdot \delta\mathbf{x} + \mathbf{G} \cdot \mathbf{w} \tag{3.1-2}$$

with:

$\delta\mathbf{x}$ error states

$\mathbf{F}$ dynamics matrix

$\mathbf{G}$ shaping matrix

$\mathbf{w}$ forcing noise (white Gaussian).

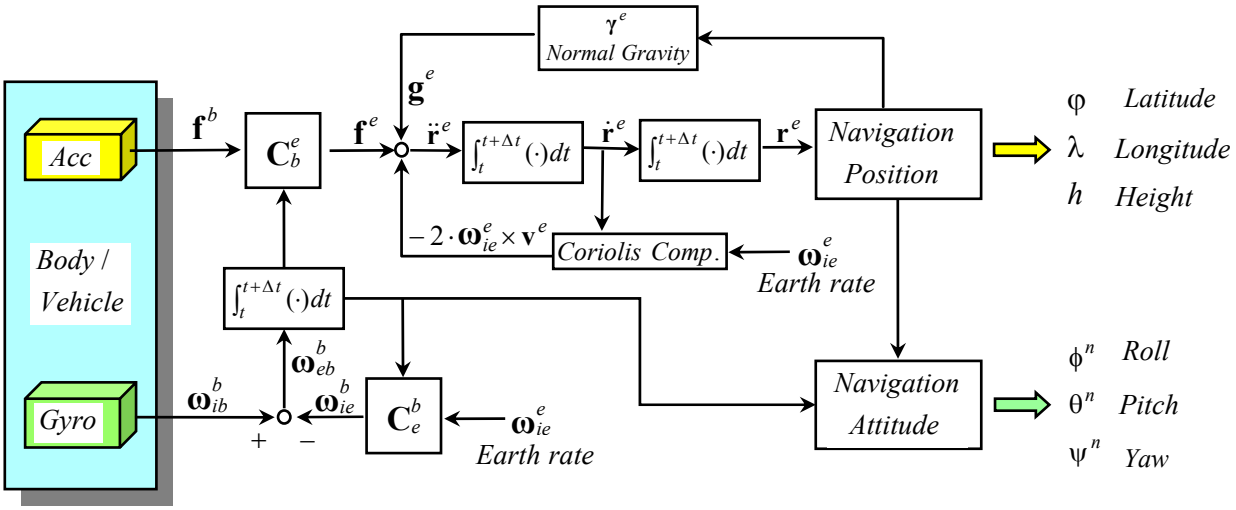

Fig. 17 *Strapdown mechanization in the e-frame*

The explicit form of the error state equations is *[Schwarz, 2001]*:

$$\begin{bmatrix} \delta\dot{\mathbf{r}}^e \\ \delta\dot{\mathbf{v}}^e \\ \dot{\boldsymbol{\varepsilon}}^e \\ \dot{\mathbf{d}} \\ \dot{\mathbf{b}} \end{bmatrix} = \begin{bmatrix} \delta\mathbf{v}^e \\ \mathbf{N}^e\delta\mathbf{r}^e - 2\boldsymbol{\Omega}_{ie}^e\delta\mathbf{v}^e - \mathbf{F}^e\boldsymbol{\varepsilon}^e + \mathbf{C}_b^e\mathbf{b} \\ -\boldsymbol{\Omega}_{ie}^e\boldsymbol{\varepsilon}^e + \mathbf{C}_b^e\mathbf{d} \\ -\boldsymbol{\kappa}\mathbf{d} + \mathbf{w}_d \\ -\boldsymbol{\beta}\mathbf{b} + \mathbf{w}_b \end{bmatrix} \tag{3.1-3}$$

with:

$\delta\mathbf{r}^e$, $\delta\mathbf{v}^e$:	position, resp. velocity error states
$\boldsymbol{\varepsilon}^e$:	attitude error states
$\mathbf{N}^e$:	coefficient matrix relating normal gravity errors to position errors (see eq. 3.1-4)
$\mathbf{F}^e$:	skew-symmetric matrix corresponding to the specific-force vector in *e*-frame $\mathbf{f}^e = \mathbf{C}_b^e\mathbf{f}^b$
$\mathbf{b}$:	vector of residual accelerometer bias errors, given in the body frame
$\mathbf{d}$:	vector of residual gyro drift errors, given in the body frame
$\boldsymbol{\beta}$, $\boldsymbol{\kappa}$:	diagonal matrices containing the inverse of the correlation times for the Gauss-Markov first order stochastic noise-process models
$\mathbf{w}_b$, $\mathbf{w}_d$:	vectors of white noise.

The explicit expression of the coefficient matrix $\mathbf{N}^e$:

$$\mathbf{N}^e = \frac{kM}{(\mathrm{r}^e)^3}\begin{bmatrix} -1+3\dfrac{(x^e)^2}{(\mathrm{r}^e)^2} & 3\dfrac{x^e y^e}{(\mathrm{r}^e)^2} & 3\dfrac{x^e z^e}{(\mathrm{r}^e)^2} \\ 3\dfrac{y^e x^e}{(\mathrm{r}^e)^2} & -1+3\dfrac{(y^e)^2}{(\mathrm{r}^e)^2} & 3\dfrac{y^e z^e}{(\mathrm{r}^e)^2} \\ 3\dfrac{z^e x^e}{(\mathrm{r}^e)^2} & 3\dfrac{z^e y^e}{(\mathrm{r}^e)^2} & -1+3\dfrac{(z^e)^2}{(\mathrm{r}^e)^2} \end{bmatrix} + \begin{bmatrix} (\omega_{ie}^e)^2 & 0 & 0 \\ 0 & (\omega_{ie}^e)^2 & 0 \\ 0 & 0 & 0 \end{bmatrix}, \tag{3.1.4}$$

which accounts for the errors of the normal gravity vector $\delta\boldsymbol{\gamma}^e$ due to position errors $\delta\mathbf{r}^e$ ($\delta\boldsymbol{\gamma}^e = \mathbf{N}^e\delta\mathbf{r}^e$), is derived in [*Schwarz, 2001*] by differentiating the approximation relation for the normal gravity vector:

$$\boldsymbol{\gamma}^e = -\frac{kM}{(\mathrm{r}^e)^3}\cdot\mathbf{r}^e - \boldsymbol{\Omega}_{ie}^e\cdot\boldsymbol{\Omega}_{ie}^e\cdot\mathbf{r}^e, \tag{3.1.5}$$

where:

$k = 6.673\cdot10^{-11}$ $\mathrm{m}^3/\mathrm{kg}\cdot\mathrm{s}^2$ is the Newton's gravitational constant

$M = 5.973\cdot10^{24}$ kg is the mass of the earth (deduced from the product-value: $kM = 3.986005\cdot10^{14}$ $\mathrm{m}^3/\mathrm{s}^2$, defined in the WGS 84 earth model)

$\mathbf{r}^e = [x^e \quad y^e \quad z^e]^T$ is the position vector in the Cartesian ECEF reference system.

The above equations-set (3.1.3) consists of three principal error models: the *navigation solution error vector* $[\delta\dot{\mathbf{r}}^e \quad \delta\dot{\mathbf{v}}^e \quad \boldsymbol{\varepsilon}^e]^T$, the *accelerometers measurement error vector* **b** and the *gyros measurement error vector* **d**.

For precision navigation solutions one can also model the *gravity uncertainty vector* $\delta\mathbf{g}^e$ (which, in fact, is not an error, representing the difference between the actual gravity and the normal gravity model):

$$\delta\mathbf{g}^e = \mathbf{g}^e - \boldsymbol{\gamma}^e . \qquad (3.1.6)$$

With only a supplementary Kalman filter state for the vertical-component of the gravity anomaly *[Chatfield, 1997]*, modelled as a Random-Walk noise process *[Bastos et al., 2002]*, good results, in agreement with precise air and marine gravimetric determinations, are reported.

3.2. Post-processing navigation solutions

3.2.1. Calibration and parameter identification

For the implementation of the navigation program, one must use appropriate calibration values (for the scale factors, sensor axes misalignments and for removal of the main part of the inertial sensor errors: biases and temperature dependencies); one needs also to determine the parameters of the modelled error processes (e.g., some residual sensor biases, or the correlation time of the stochastic noise models). The principal part of this information is furnished by the manufacturer, in our case iMAR, as a result of a calibration process, and it is used directly in the SIMU software to calibrate the measurement values. Through own calibrations – using the Kingspad navigation program for residual bias estimation or RAV (Root Allan Variance) diagrams *[IEEE Std. 647-1995, App. C]*, PSD (Power Spectrum Density) representations and Autocorrelation functions for sensor noise analysis (estimation of the

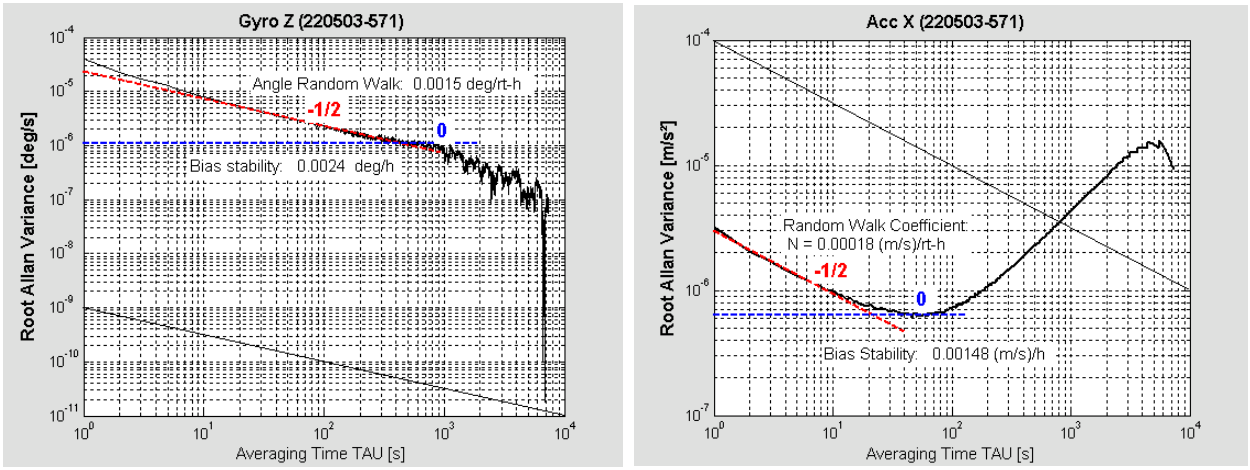

a. *gyroscope* **b**. *accelerometer*

Fig. 18 *Root Allan-Variance for the noise-data of the z-axis gyroscope and the x-axis accelerometer*

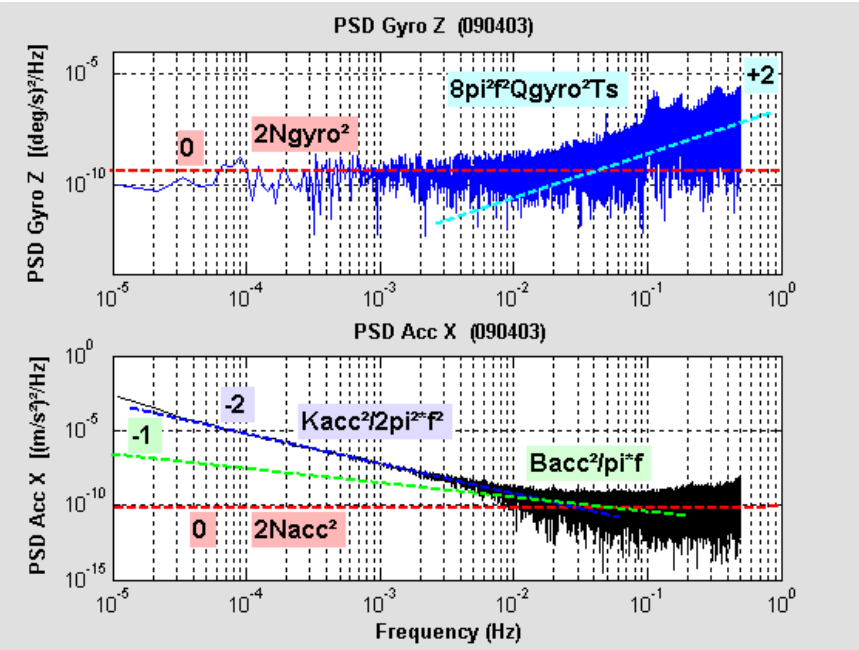

Random-Walk process parameters, least-squares fitting to derive the parameters of time-correlated noise processes of first order Gauss-Markov (G-M) type or estimations of the bias instability and quantization noise) – we could improve the navigation solution of our SIMU. Fig. 18 shows some results from the determination of the Random Walk and Bias Stability using the Allan Variance diagrams (program written in Matlab©).

Fig. 19 *PSD diagrams for GG1320 Laser gyroscope and QA2000 balancing accelerometer*

The noise data were first decimated from 100 Hz to 1 Hz (with simultaneous low-pass filtering); for comparison with values as they are usually given in the literature, we have converted some measuring unities for the gyro and accelerometer results respectively. We have obtained values of $0.0015\ \text{deg}/\sqrt{\text{h}}$ and $0.3\,\mu\text{g}/\sqrt{\text{Hz}}$ for the Random Walk coefficients, resp. 0.0024 deg/h and 0.06 μg for bias instability (the accelerometer noise values are a bit too optimistic – compare Tab. 1 – because of the analog anti-aliasing filter used by SIMU). From the accelerometer RAV diagram one can see the dominating long term drift process (due, e.g., to temperature variations) for averaging times larger than about 100 s.
The performance limit for the inertial navigation sensors can be also derived from the PSD functions (periodograms, for finite data lengths) of the sensor noise. It is presented in Fig. 19. This representation, complementary to the Allan Variance diagram, permits the easy estimation of, e.g., Random Walk Noise and of the Quantization Noise for the Laser gyroscopes and balancing accelerometers.
One can also derive the noise standard deviation of a zero-mean signal, for the measurement frequency bandwidth Δf, employing the periodogram values for the PSD function $S(f)$ as in the expression (3.2.1-1), where the integration is carried out only for the positive frequencies:

$$\sigma^2_{noise} = 2 \cdot \int_{f_1}^{f_1+\Delta f} S(f) \cdot df \ . \qquad (3.2.1\text{-}1)$$

For a frequency bandwidth of, e.g., 10^{-2} to $5 \cdot 10^{-1}$ Hz, one has a noise standard deviation: $\sigma_{noise} \approx 1$ μg (= 1 mGal).

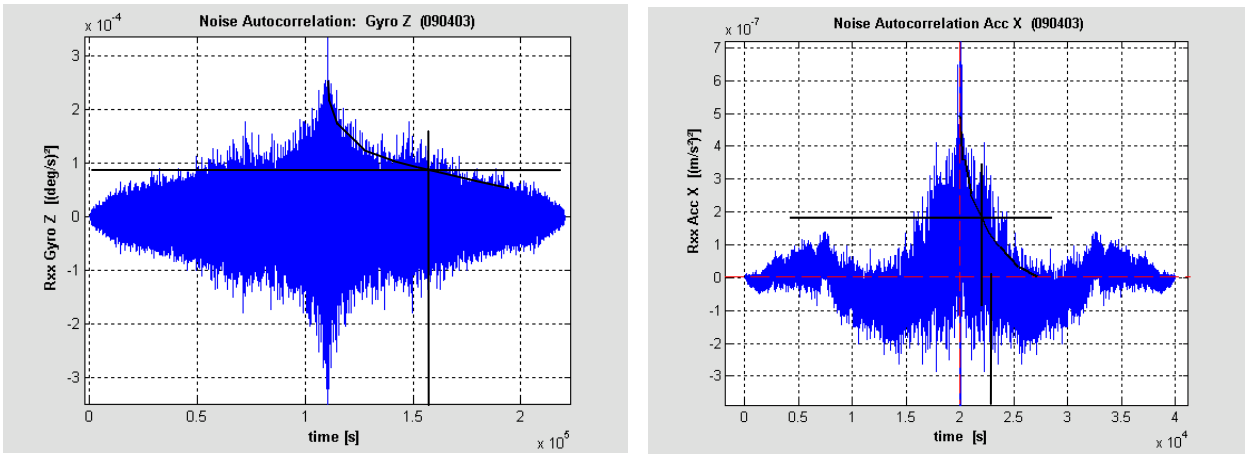

a. *Gyroscope Z* **b**. *Accelerometer X*

Fig. 20 *Autocorrelation functions for the time-correlated noise processes of Laser-gyroscopes and accelerometers*

Using the sampling period Ts = 1 s for the noise measurement made under laboratory conditions, we obtain graphically for the Z-gyro and X-accelerometer the values $0.001\ \text{deg}/\sqrt{\text{h}}$ and $0.5\,\mu\text{g}/\sqrt{\text{Hz}}$ for the angle and velocity Random Walk coefficients respectively, 0.3 μg for accelerometer Bias Instability, 0.2 μg for the acceleration Random Walk and 0.25 arcsec/s for the gyro Quantization Noise coefficient (in agreement with the value of $\frac{1}{\sqrt{12}} \cdot \text{LSV}$, where $\text{LSV} \approx 1$ arcsec represents the least significant value (angle resolution) derived from the registered rate data).
In Fig. 20 the autocorrelation functions for gyro and accelerometer noise are presented (the data were recorded in stationary operation, under laboratory conditions). From the diagrams 20-a (a first order Gauss-Markov gyro noise process) and 20-b (the accelerometer noise – a second order G-M process *[Maybeck, 1982]* – was also approximated as a first order G-M process, so adopted from modelling constraints reasons (see equations 3.1-3)), we estimate the correlation times (t_{corr}) of the noise stochastic processes to 11 h for Laser gyroscopes and 0.5 h for the balancing accelerometers. (A rapid graphical evaluation of the correlation times for the two G-M noise processes is made considering the points with the coordinates [t_{corr}, *P(0)/e*] by the autocorrelation diagrams in Fig. 20).

3.2.2. Kingspad-software input/output parameters

The used post-processing software, originated from the University of Calgary (**KINGSPAD™** : **KIN**ematic **G**eodetic **S**ystem for **P**ositions and **A**ttitude **D**etermination, see also the Website *http://www.uti.ca/kingspad.htm*), integrates the GPS/INS data by means of an optimal Kalman filter, with the aim of delivering a corrected position and attitude trajectory solution, without the specific drawback of each system: the GPS data set discontinuities, caused by cycle-slips or antenna shadings, respectively the time-growing INS errors.

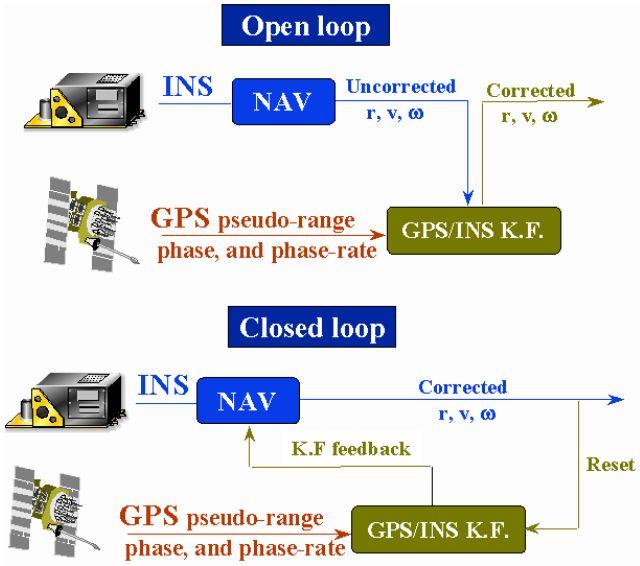

Fig. 21 *GPS/INS integration strategies in the Kingspad Software, from [http://www.uti.ca/kingspad.htm]*

In principle, one can choose between two implementation strategies for the Kalman filter: the first one, the centralized filter approach (tight-coupling), uses a common state vector for GPS and INS error modelling, the INS solution constituting the reference trajectory solution and the GPS measurement updates being used to estimate the global state solution.
The second one, the de-centralized filter approach (loose-coupling), chosen for the Kingspad software, has net speed and data integrity advantages (furthermore, aloud tests presented in literature, little accuracy differences between the two approaches could be proven). It runs simultaneously separate INS and GPS Kalman filters, the latter one being used also as update for the INS one. The software provides special bridging procedures for the GPS-outages periods and permits also to choose the open-/closed-loop correction strategy (see Fig. 21).
In Fig. 22 the data-sources needed for the post-processing and the solution building with the Kingspad software are shown. The principal input/output data constituents are given below explicitly (for a detailed description of all data sets see the Website: *http://www.uti.ca/kingspad-reference-guide.pdf*):

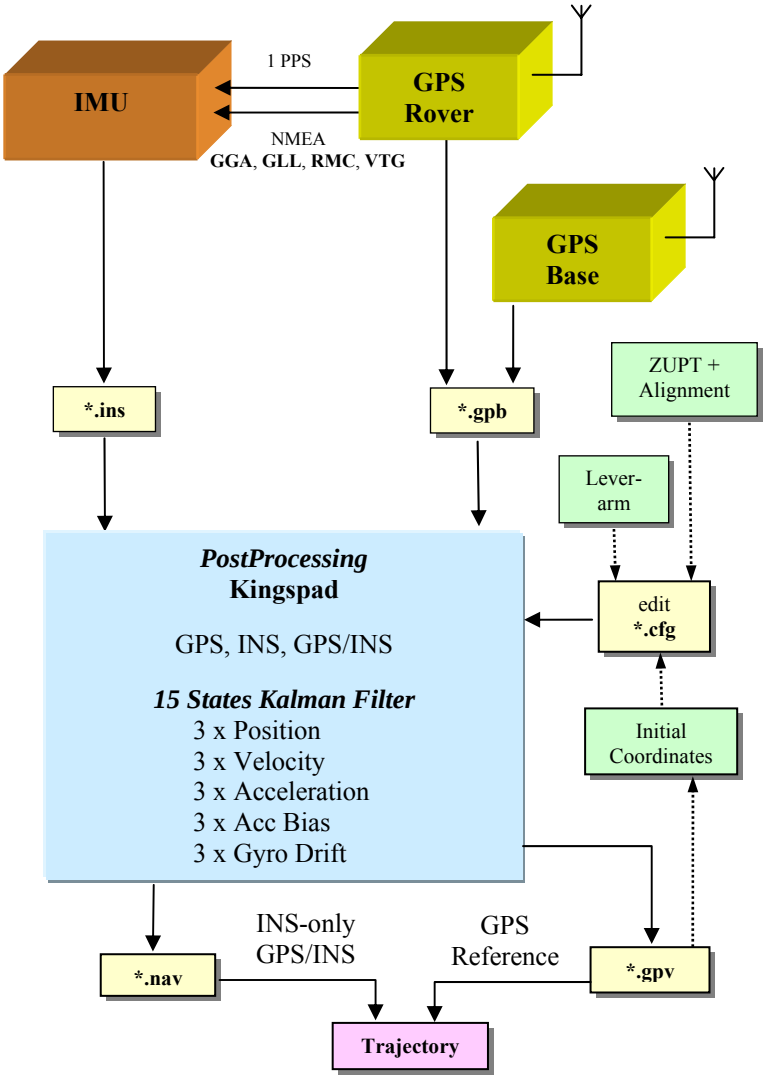

Fig. 22 *Post-processing with Kingspad software*

Inputs:

- **GPS data** converted in Kingspad ***.gpp** and ***.epp** formats
- **IMU data** in Kingspad ***.ins** format

The calibrated IMU inertial data (e.g., the variables: TMOD, TIME, IACC, IOMG, NRPY, TEMP) are stored in a binary file; the effective vectors used from Kingspad software are: **TMOD, IACC, IOMG**. The TIME and NRPY values are used only for comparison purposes; the TEMP values are eventually used for off-line compensation of residual temperature correlations.

The significance of these variables is:

TMOD: time model, a time scale in [SoD], continuously updated by external GPS-PPS pulses

TIME: IMU's time in [s]

IACC: inertial acceleration vector (specific force vector): $[\, f^b_{ib_x} \quad f^b_{ib_y} \quad f^b_{ib_z} \,]^T$ in [m/s²]

IOMG: inertial rotation rate vector: $[\, \omega^b_{ib_x} \quad \omega^b_{ib_y} \quad \omega^b_{ib_z} \,]^T$ in [deg/s]

NRPY: Roll, Pitch, Yaw rotation angles (*body*-frame to ENU-frame) in [deg], calculated on-line in the SIMU module

TEMP: ISA's (Inertial Sensor Assembly) temperature in [K]

- Supplementary information for processing purposes, furnished by editing of the configuration Kingspad-file ***.cfg**:
  - INS Initial Position, ZUPTs, Alignment, Timing
  - GPS processing directives, Timing
  - Kalman Filter covariances
  - Supplementary Gyro and Accelerometer bias offsets, as well as the correlation times for the first order Gauss-Markov stochastic noise-process models of the inertial sensors
  - Lever-arm between the SIMU's *body*-frame reference point (marked on the SIMU case) and the centre-of-phase of the GPS antenna (offsets are expressed in *b*-frame coordinates).

Outputs:

- A set of binary / ASCII solution files, the most important of them being:
  - ***.nav**: ASCII file containing the **INS navigation outputs** every second (INS position, velocity and attitude)
  - ***.att**: ASCII file containing the **INS attitude** (after Kalman filter update)
  - ***.gpv**: ASCII file containing the **GPS position and velocity** outputs (referenced at the GPS antenna centre)
- ***.cal**: ASCII calibration file (Kalman Filter estimated biases)
- ***.fil**: ASCII file with position, velocity and attitude for optimal smoothing
- ***.qcf**: quality control files
- ***.rep**: a processing report file.

3.2.3. Indoor navigation experiment

In order to put into evidence some trajectory-solution improvements by using supplementary bias corrections, respectively zero velocity updates (ZUPTs), we have conducted a first indoor INS-only navigation experiment, with only ZUPT updates, upon a perimeter of about 200 m on the floor of our University.

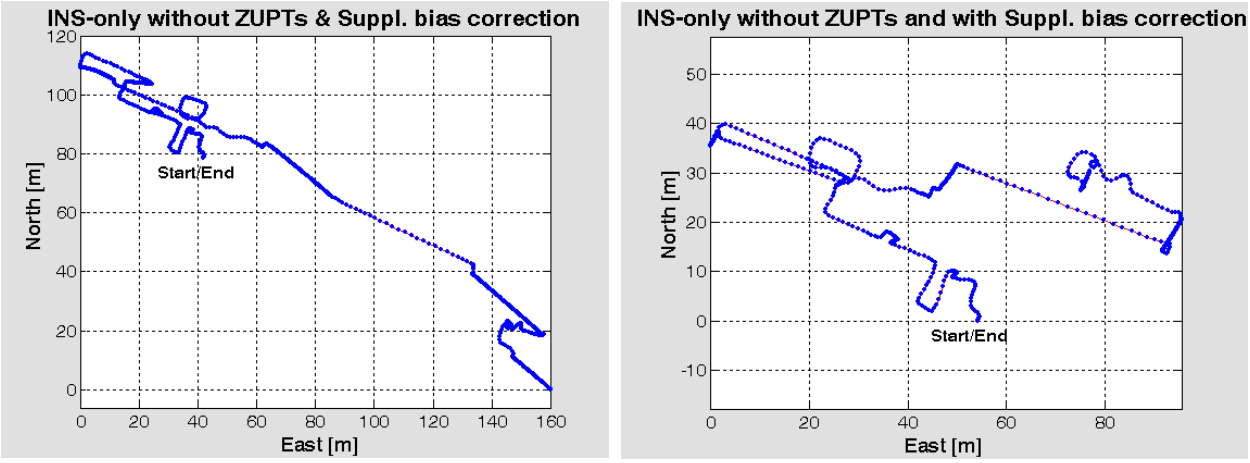

a. ***INS-only** trajectory **without ZUPTs** and **without supplementary bias correction***

b. ***INS-only** trajectory **without ZUPTs** and **with supplementary bias correction***

Fig. 23 ***INS-only** trajectories processed **without ZUPTs** and **with/without** supplementary **bias correction***

Fig. 23-a shows the INS-only solution without any supplementary bias corrections or updates. Comparing this figure with the final solution from Fig. 24, one can observe great trajectory errors, appearing as a consequence of the uncompensated residual offsets and drifts, that make the solution unusable. A first improvement step, that consists in the compensation of sensor bias offsets, shows a certain amelioration of the trajectory solution (see Fig. 23-b), but still insufficiently without the use of the zero velocity updates. The residual offset correction values, which bring in fact an additionally offset compensation to the offsets attended in the standard calibration file used by the IMU's pre-processing software, were taken from a Kalman filtering estimation of the inertial sensor biases for an earlier GPS/INS navigation-session processing, outputted in the Kingspad file of the type *.cal. Taking into account both compensation techniques (supplementary offset compensation and ZUPTs) one obtains quite precise INS-only solutions (see Fig. 24) (e.g., position difference between the Start/End points of the closed trajectory lies in the decimeter range), also for relatively long navigation durations, superior to some fractions of hour - in our case, the navigation duration (without to consider the alignment phase) was about 28 min.

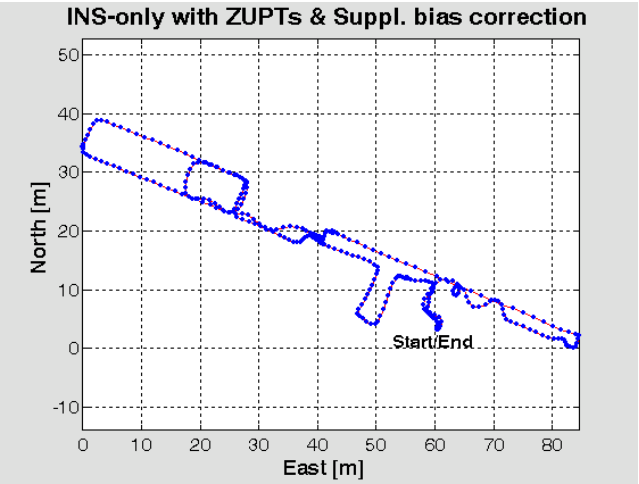

Fig. 24 ***INS-only*** *trajectory processed* ***with*** *ZUPTs* ***and*** *supplementary bias correction*

For the final solution, in the presence of the additional bias compensation, the amount of the velocity tolerance, given as input in the Kingspad software for the ZUPT updates, could be lowered for one order of magnitude: from 0.12 m/s to 0.012 m/s; so, the Kalman filtering estimation sequence for the alignment became much more accurate.

3.2.3. Land-navigation experiments (car-drive)

For land-navigation experiments we have chosen an open area in order to obtain a continuous DGPS solution, used as *reference* for comparison with the INS-only solutions with/without zero-velocity updates, or with the integrated GPS/INS one. The 1 Hz GPS updates of the integrated solution provide a calibration of the inertial system (data acquisition rate of 100…500 Hz) during the mission itself (in our case, in off-line modus). The inertial sensors orientation and the precise short-term position and velocity information could be used for cycle-slip detection and correction. The following figures present some evaluation results, derived by partial or total use of external update information.

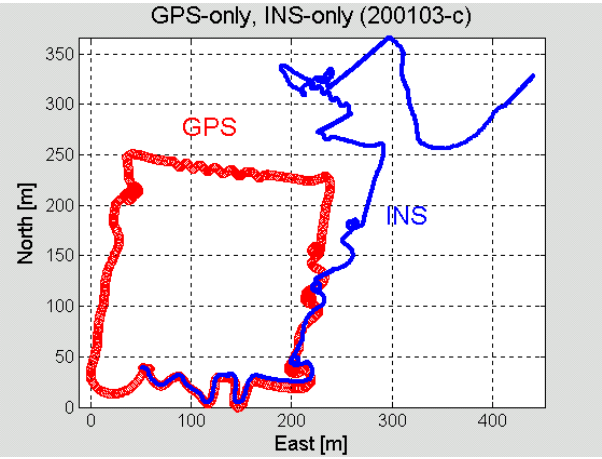

a. *GPS-only (reference) and INS-only trajectories*

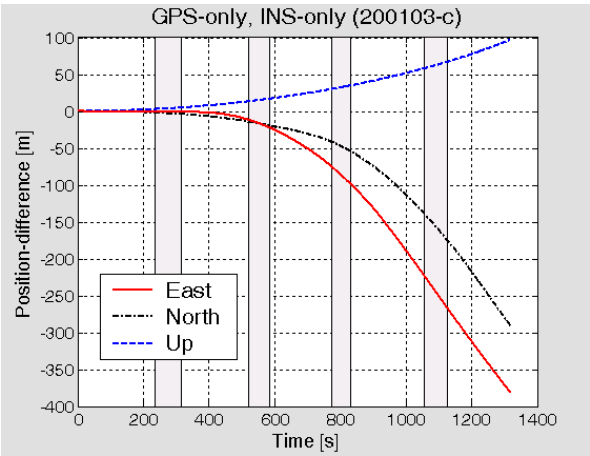

b. *Position differences between GPS-only (reference) and INS-only trajectories*

Fig. 25 ***INS-only*** *and GPS-only (reference) trajectories*

In Fig. 25-a the reference DGPS continuous trajectory (marked each second with *circles)* and the INS-only trajectory (marked also at each second with *points*) are shown. The only update is made at the beginning, through the about 10 min. alignment. Thereby, during the coarse and fine alignment phases the initial IMU orientation in the ENU *n*-frame is estimated and some turn-on to turn-on biases are corrected. The lack of updates during the mission causes trajectory errors, produced principally through the integration of residual biases of rates and specific-forces. The position errors, computed as differences between the INS trajectory and the reference DGPS one, are presented in Fig. 25-b; the parabolic shape of these errors shows some quadratic and cubic dependencies, that could be put in

relation with integration processes, simply illustrated by the following time-dependency formulas, which consider only the residual biases *[Titterton et al., 1997]*:

$$\delta Position_{bias\ acc} = \frac{1}{2} \cdot \delta b_{acc} \cdot t^2 \qquad (3.2.2\text{-}1)$$

$$\delta Position_{bias\ gyro} = \frac{1}{6} \cdot g \cdot \delta b_{gyro} \cdot t^3 . \qquad (3.2.2\text{-}2)$$

The gravity-compensation bias term $g \cdot \sin \varepsilon_{angle\ bias}$ is approximated here, for reduced angle-biases, by the expression $g \int \delta b_{gyro} \cdot dt$.

However, the interpretation through the direct use of such simple relations is not possible for the East/North trajectory components, because of the repeated interchange of the orientation of the body x- and y-axis with respect to the navigation axes during the mission. An important improvement was achieved through the compensation of

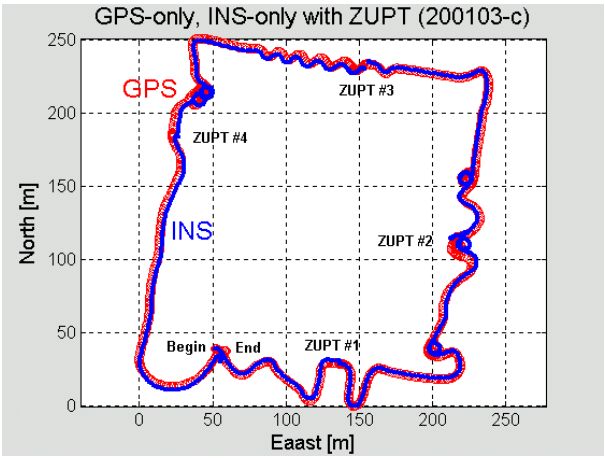

a. *GPS-only (reference) and INS-only with ZUPT trajectories*

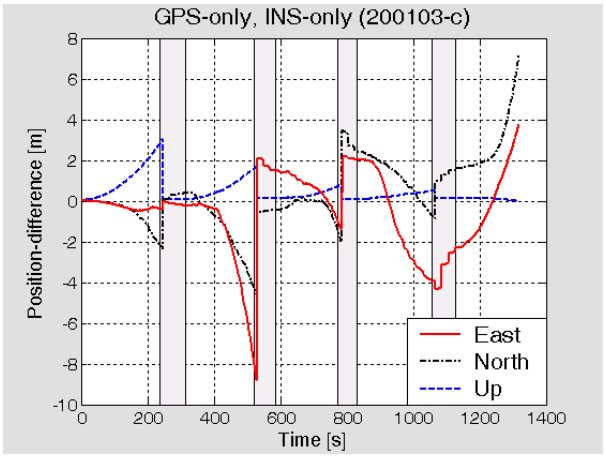

b. *Position-difference between GPS-only reference and INS-only with ZUPT trajectories*

Fig. 26 ***INS-only with ZUPT*** *and GPS-only (reference) trajectory*

constant biases, using a set of predetermined values, delivered in the post-processing solution.

In the next step we have made use of the ZUPT information, a common practice in the case of geodetic applications with no GPS update possibilities, like, e.g., tunnel surveying. Comparison of Fig. 25 and 26 shows the improvement produced only by employing four ZUPTs along the mission track; the characteristic "learning" capability of Kalman filtering is nicely illustrated for the vertical channel (Fig. 26-b): one sees the time-accumulated error diminishing after each zero-velocity update.

The insufficient observability of the Kalman filtering estimation process by ZUPT-only updates could be compensated through simultaneous coordinate updates (CUPTs) during the same ZUPT periods, so achieving further INS-only trajectory-precision improvements.

For the completion of evaluation, an integrated DGPS/INS solution has been computed, with GPS updates every second. The results – trajectory and differences in comparison to the DGPS reference solution – are depicted in Fig. 27; the errors (differences) shown in Fig. 27-b, with *sub-centimeter* 1-sigma values (for example: 0.005 m for the additionally bias-compensated vertical channel) presents, of course, essentially lower values during the stationary

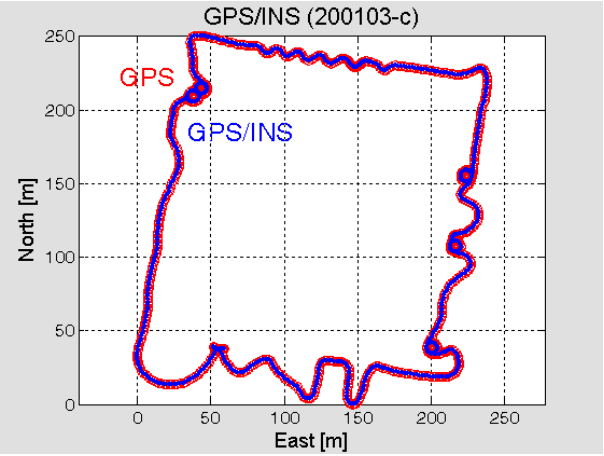

a. *GPS-only (reference) and* ***GPS/INS integration*** *trajectories*

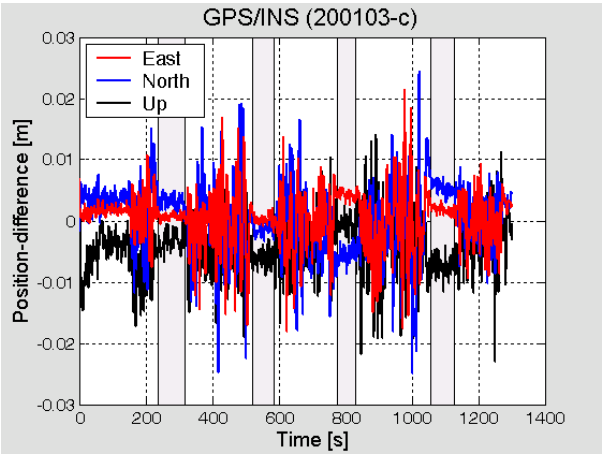

b. *Position-difference between GPS-only reference and GPS/INS trajectories*

Fig. 27 ***GPS/INS integration*** *and GPS-only (reference) trajectories*

ZUPT periods. The continuous GPS coordinate-updates made in the post-processing Kalman filtering improves also the estimation of other filter variables, making the use of SIMU an option for accurate geodetic measurements, like scalar or vectorial gravimetry.

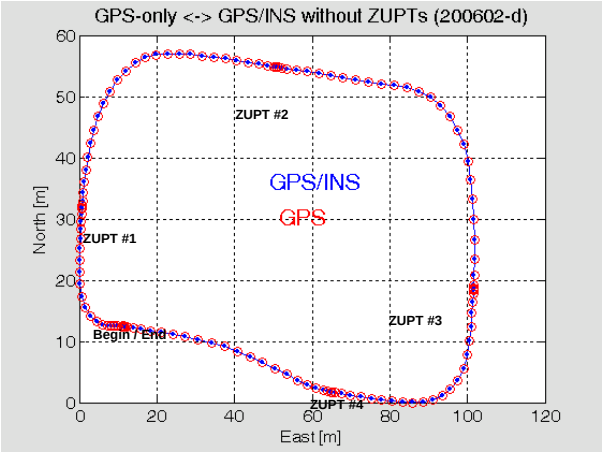

a. *GPS-only (reference) and* ***GPS/ INS integration*** *trajectories*

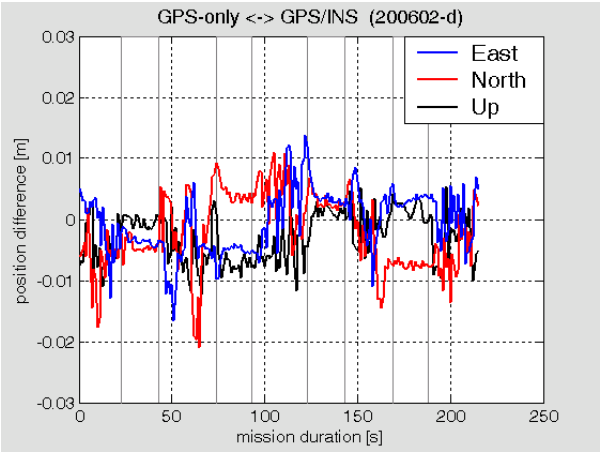

b. *Position-difference between GPS-only reference and GPS/INS trajectories*

Fig. 28 ***GPS/INS integration*** *and GPS-only(reference) for a low-dynamics trajectory*

The position-difference errors strongly depend on the drive dynamics, especially during curved trajectory portions: some errors in the roll, pitch angles cause accelerometer bias errors, through a wrong gravity compensation, whereas heading errors induce biases of the accelerometers along the drive-axis. Comparatively, one can see the precision differences between the intensive-dynamics trajectory in Fig. 27 and the low-dynamics trajectory in Fig. 28.

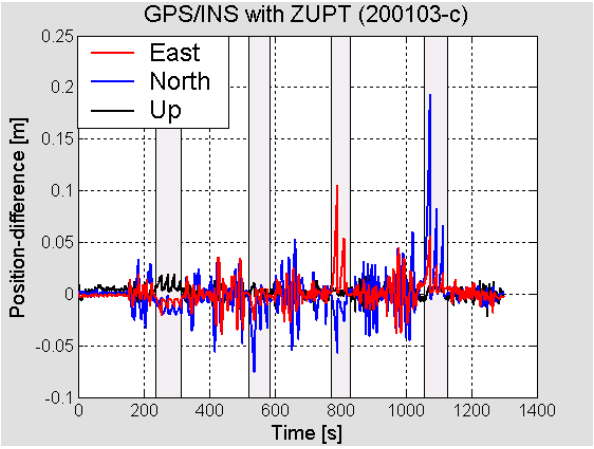

a. *GPS/INS without GPS update during the ZUPT periods*

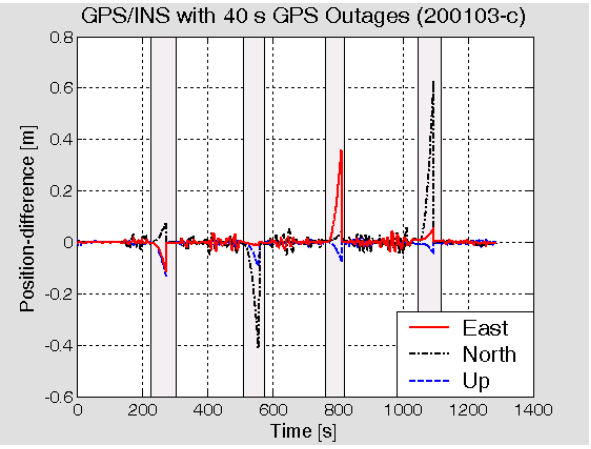

b. *GPS/INS with simulated 40 s GPS outages during the car rest*

Fig. 29 *Position-differences for GPS/INS solution with ZUPTs and simulated* ***40 s GPS outages***

Showing in Figure 29-a the position-differences during the car-rest (differences between the reference GPS-only trajectory and the integrated GPS/INS trajectory, with only four ZUPT updates, but without GPS update during the ZUPT periods), one can also observe the "learning" capability of the Kalman filter integration, the differences inside the ZUPT periods being lower time after time.

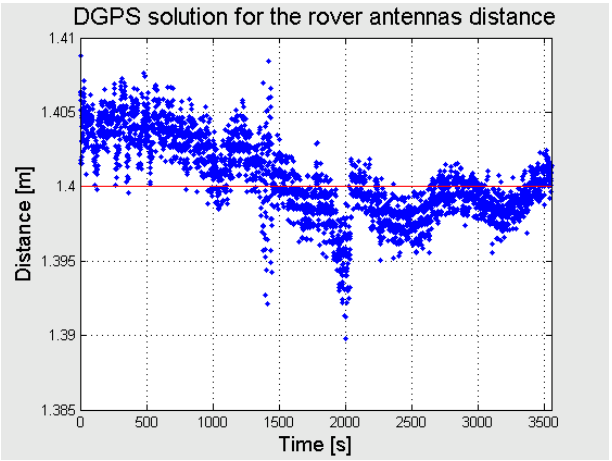

Simulation results for 40 s GPS outages, produced during stationary periods of the vehicle (however, after a GPS/INS integration period, which is in principle equivalent to a calibration sequence) are presented in Fig. 29-b; for the *z*-axis accelerometer, additionally corrected for bias-offset, the differences remain under 15 cm. The two other accelerometers were used only with their initial calibration bias offset: the errors are nevertheless under 0.7 m, for both of them, after GPS outages of 40 s.

A measure for the precision of the kinematic DGPS solution is given by comparing the fixed distance of 1.40 m

Fig. 30 *DGPS solution of the constant distance (1.40 m) between the two rover antennas*

between the two rover-antennas (see the horizontal line in Fig. 30) with the DGPS solution for these distance, determined from two independent OTF solutions *[see also: Dorobantu et al., 1999]*; one can see the good precision of the GPS solution, the standard deviation of the relative position error for the two rover antennas not exceeding 0.27 cm.

4. Conclusions and recommendations for further investigations

The paper discusses the main problems encountered by use of a navigation-grade SIMU for precise measurements: parameter determination for the inertial sensor models, methods of increasing the post-processing accuracy for inertial-only or integrated GPS/INS solutions, as well as evaluation through laboratory or field experiments, which use as reference a precise, uninterrupted DGPS trajectory solution. After a brief presentation of the problems of sensor error modelling and strapdown navigation, some results from the effectuated field tests are commented. Using the specialized post-processing software Kingspad and its capability to improve the initial calibration parameters, we were able to maintain trajectory errors in the *cm* level for the integrated solution, resp. in the *meter* range for the INS-only solution with zero-velocity updates. Compared to our low-cost IMU *[Dorobantu et al., 1999]*, the precision of the RLG-SIMU is about two orders of magnitude better. Further increase in precision could be achieved by an improved temperature compensation model for the SIMU's accelerometers.
The results obtained show that our SIMU can be used for precision navigation or surveying applications. Through the future increasing of the data acquisition rate and by using adequate filtering procedures – notch filters for the dithering-frequencies (also using of the special feature of the SIMU of per-software decoupling of the dithering for short static periods), long-period zero-phase digital FIR filters, as well as smoothing procedures – we envisage to achieve a qualified precision gravity-measurement inertial unit.
To achieve higher flexibility in the determination of specific variables (like, e.g., the gravity anomaly δg), as well as to increase the navigation solution precision (inherently improving also the sensor-outputs precision), we intend to write our own strapdown-navigation/Kalman-filtering software, with obvious capability to model additional error states.
An extended report about calibration works and smoothing results will be presented in a separate work.

Acknowledgments: The authors acknowledge the continuous support of Prof. R. Rummel, since the specification phase of the SIMU, and express the gratitude to Prof. K.P. Schwarz and his co-workers for fruitful discussions about the optimal use of the Kingspad software. Special thanks go to iMAR (Dr. E. v. Hinüber, Dipl.-Ing. M. Petry, Dr. J. Schäfer), for their support in the correct use of the SIMU and for the openness to our special demands.

5. References

AlliedSignal (1998): "*Model QA2000 Accelerometer; Product specification*", AlliedSignal Aerospace, USA
Aronowitz, F. (1999): "*Fundamentals of the Ring Laser Gyro*", in: "Optical Gyros and their Application", RTO AGARDograph 339
Bastos, L., Tomé, P., Cunha, T., Fernandes, M., J., Cunha S. (2002): *"Gravity anomalies from airborne measurements – experiments using a low cost IMU device*", in Sideris, M. G. (ed.), International Association of Geodesy Symposia, Springer, Vol.123, pp. 253-258.
Bose, S., C. (2000): "*Lecture Notes on GPS/INS Integrated Navigation Systems*"**,** Technalytics Inc., CA, USA
Chatfield, A., B. (1997): " *Fundamentals of High Accuracy Inertial Navigation* ", Amer. Inst. of Aeronautics and Astronautics, Inc.
Dorobantu, R., Zebhauser, B. (1999): "*Field Evaluation of a Low-Cost Strapdown IMU by means GPS*", Ortung und Navigation 1/1999, DGON, Bonn
Dorobantu, R., Gerlach, Ch. (2004): "*Characterisation and Evaluation of a Navigation-Grade RLG SIMU*", European Journal of Navigation, Vol. 2, No. 1, February 2004
Farell, J., A., Barth, M. (1999): " *The Global Positioning System and Inertial Navigation* ", McGraw-Hill, NY
Grewal, M., S., Weill, L., R., Andrews, A., P. (2000): „*Global Positioning Systems, Inertial Navigation, and Integration*", John Wiley & Sons
Hua, C. (2000): "*Gyrocompass Alignment with Base Motions: Results for a 1 nmi/h INS/GPS System*", Navigation, Vol. 47, No. 2, 2000
*** IEEE Std. 337-1972**: "*Format Guide and Test Procedure for Linear, Single-Axis, Pendulous, Analog Torque Balance Accelerometer"*, IEEE Aerospace and Electronic Systems Society, USA
*** IEEE Std. 647-1995**: "*Format Guide and Test Procedure for Single-Axis Laser Gyros"*, IEEE Aerospace and Electronic Systems Society, USA
*** iMAR GmbH (2001):** "*iNAV-RQH for IAPG/GEO München: Configuration and usage*", St. Ingbert, Germany
Jekeli, Ch. (2000): "*Inertial Navigation Systems With Geodetic Applications*", Walter De Gruyter
Killpatrick, J. (1967): "*The laser gyro*", IEEE Spectrum, Oct. 1967

Krempasky, J. (1999): "*Terminal Area Navigation Using Relative GPS Bias States with a Terrain Scene*", Navigation, Vol. 46, No. 2, 1999
Macek, W., M., Davis, D., T., M. (1963): "*Rotation rate sensing with traveling-wave ring lasers*", Appl. Phys. Lett., 2, Feb. 1963
Maybeck, P., S. (1982): "*Stochastic Models, Estimation and Control*", Academic Pr.
Merhav, S. (1996): "*Aerospace Sensor Systems and Applications*", Springer-Verlag New York, Inc.
Rodloff, R. (1999): "*Physical Background and Technical Realization of Optical Gyros*", in: "Optical Gyros and their Application", RTO AGARDograph 339
Rogers, R., M. (2000): "*Applied Mathematics in Integrated Navigation Systems*", American Institute of Aeronautics and Astronautica, Inc., Reston, Virginia, USA
Savage, P., G. (1984): "*Advances in Strapdown Sensors*", AGARD (Advisory Group for Aerospace Research and Development) Lecture Series No. 133
Savage, P., G. (1997): "*Strapdown Inertial Navigation: Lecture Notes*", Strapdown Associates, Inc., MN-USA
Savage, P., G. (2000): "*Strapdown Analytics",* Vol. 1, 2, Strapdown Associates, Inc., MN-USA
Schwarz, K., P., Wei, M. (2001): "*INS/GPS Integration for Geodetic Applications*", Lecture Notes ENGO 623
Stieler, B. (1995): "*Inertial navigation*", AGARD AG-331
Titterton, D., H., Weston, J., L. (1997): "*Strapdown Inertial Navigation Technology*", IEE Books, Peter Peregrinus Ltd., UK
Torge, W., Falk, R., Franke, A., Reinhart, E., Richter, B., Sommer, M., Wilmes, H. (1999): "*Das Deutsche Schweregrundnetz 1994 (DSGN94); Band I*", Deutsche Geodätische Komission, Reihe B, Heft Nr. 309
*** Trimble Navigation Ltd. (1995)**: "*Series 4000 Receiver Reference*", Sunnyvale, CA, USA
Wertz, R., J. (1991): "*Spacecraft Attitude Determination and Control*", 7-th Edition, Kluwer Academic Publishers, Boston

Website URL references:

http://www.imar-navigation.de
http://www.inertialsensor.com/qa2000.shtml
http://www.inertialsensor.com/docs/qa2000.pdf
http://www.ais.honeywell.com/dss/sgp/products/rlg-gg1320an.htm
http://www.uti.ca/kingspad.htm
http://www.uti.ca/kingspad-reference-guide.pdf
http://www.nmea.org/
http://vancouver-webpages.com/peter/nmeafaq.txt

Appendix A: **Insight in the ISA of the SIMU**

Here some images of the used Honeywell inertial sensors are presented: accelerometers and gyroscopes, as well as the ISA's (Inertial Sensors Assembly) mechanical unit. One can see the milled locations for the two triaxial clusters and the provided elastic damping shock-mounts for the ISA suspension.

Fig. A-1 *QA2000 Honeywell balancing accelerometer: external view*

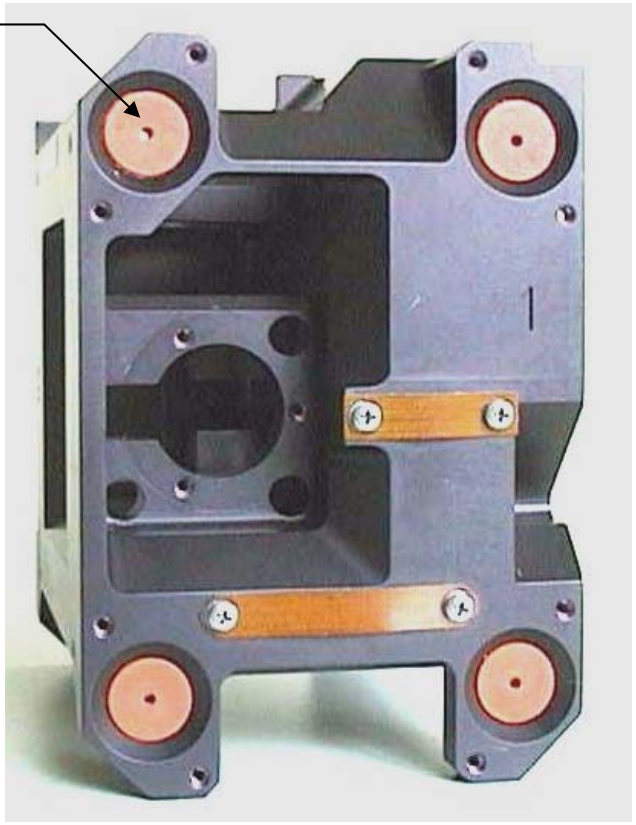

Fig. A-2 *ISA's mechanical unit: view of an accelerometer cavity*

Fig. A-3 *ISA's mechanical unit: view of a gyroscope cavity*

Fig. A-4 *GG1320 Honeywell Ring Laser Gyroscope: external view*

Appendix B: **Supplementary investigations about the static sensitivity of the SIMU**

Using a precision tilting table (180 arcsec per disc-rotation) – kindly provided by the Chair of Geodesy, TUM – and supplementary precision tilting measurements (by means of a mechanical comparator, see Fig. B-1), one investigates the outputs of accelerometer and gyroscopes submitted to static steps of tilts.

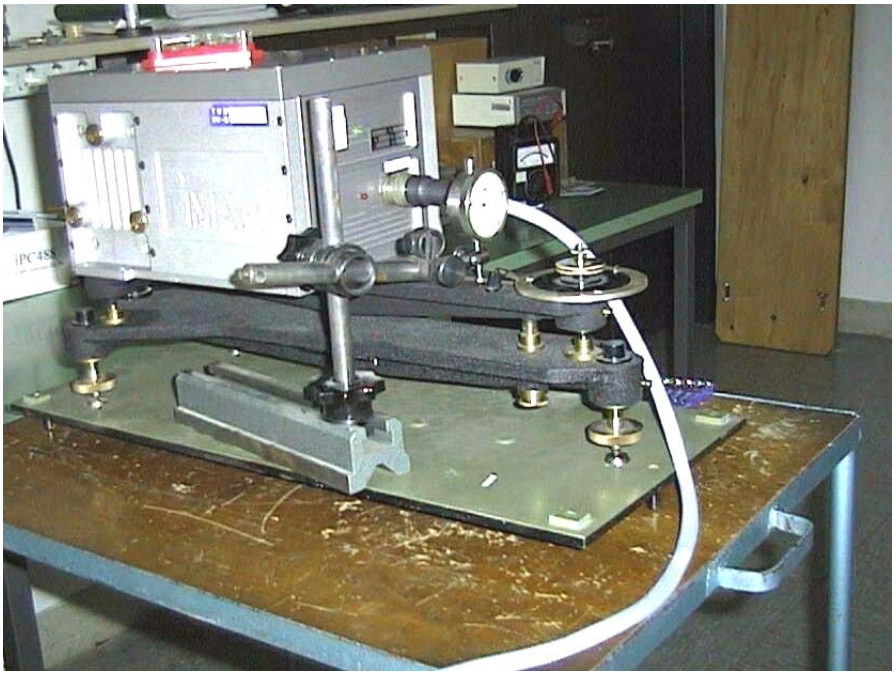

Fig. B-1 *Tilt calibration with IMU in normal position (z-axis upwards)*

Fig. B-2 *Rotated IMU on the tilting-table (y-axis upwards)*

Fig. B-3 presents the tilt-angle determination from the Laser gyroscope data: one observes the good performance of the measurement, with resolution in the arcsec range (see the zoomed area). The accompanying acceleration jumps (unfiltered static components $g \cdot \sin\theta$ of the x-axis acceleration in Fig. B-4) can be used to estimate the resolution of the acceleration-steps for static gravity measurements (using appropriate null-phase filtering of about 60 s, to eliminate the principal part of the superimposed noise from the accelerometer data, one reaches relative accuracies in the mGal range).

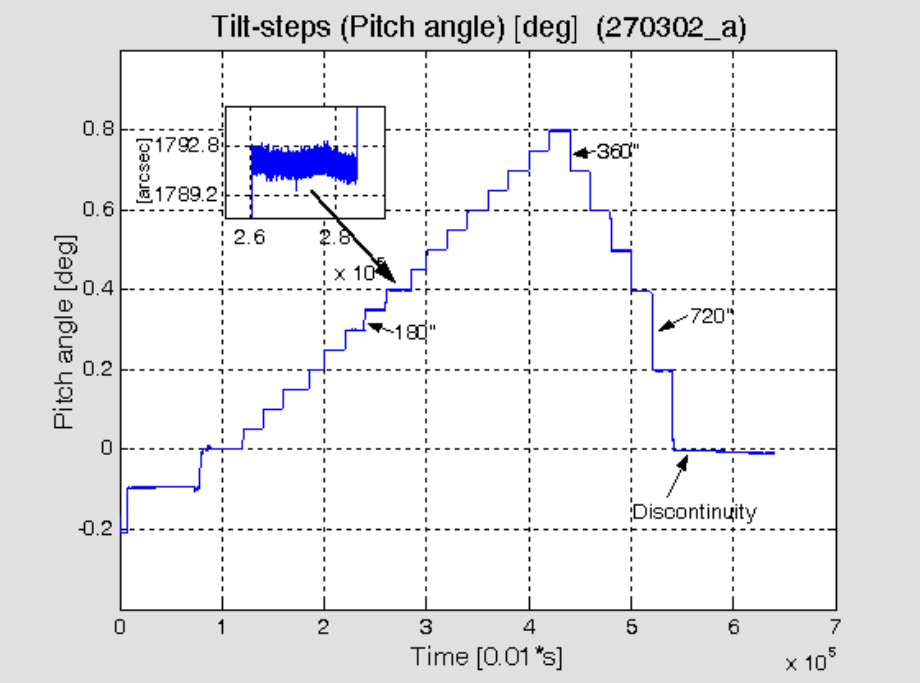

Fig. B-3 *The gyroscope-measured tilts (the tilting-table readings, in [arcsec], are also represented)*

One can also show the good agreement between the acceleration- and tilt-steps, effective for small deviations from horizontality (acceleration amplitude changes linearly with the increasing inclination in the incipient phase of deflection).

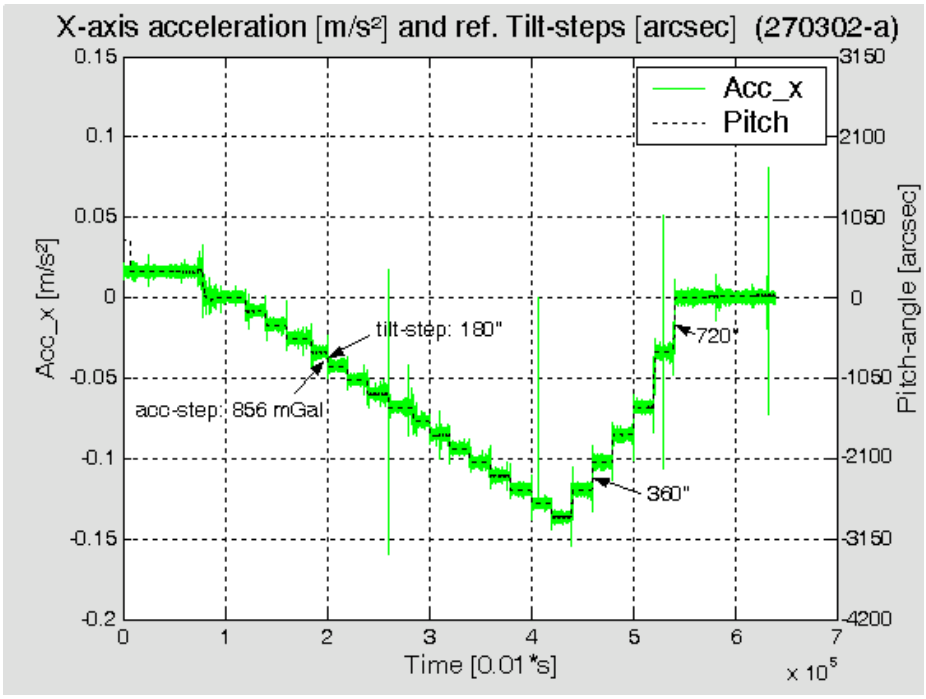

Fig. B-4 *Static unfiltered acceleration-steps together with the corresponding reference IMU tilts-steps*

Appendix C: **Investigation of an elastic damping suspension for the SIMU**

An experimental study of the damping properties of an elastic/damping rubber IMU suspension was carried out. A comparison of the PSD functions for the damped/undamped system permits an evaluation of the suspension. In our case, the rubber damper was too rigid in comparison to the own ISA's shock-mounts, so there are no significant effects. Future investigations will establish a trade-off for such a supplementary suspension, in order to assure the desired mechanical filtering of strong external vibrations, as in the case of employing the SIMU in a plane, for flight gravimetric missions.

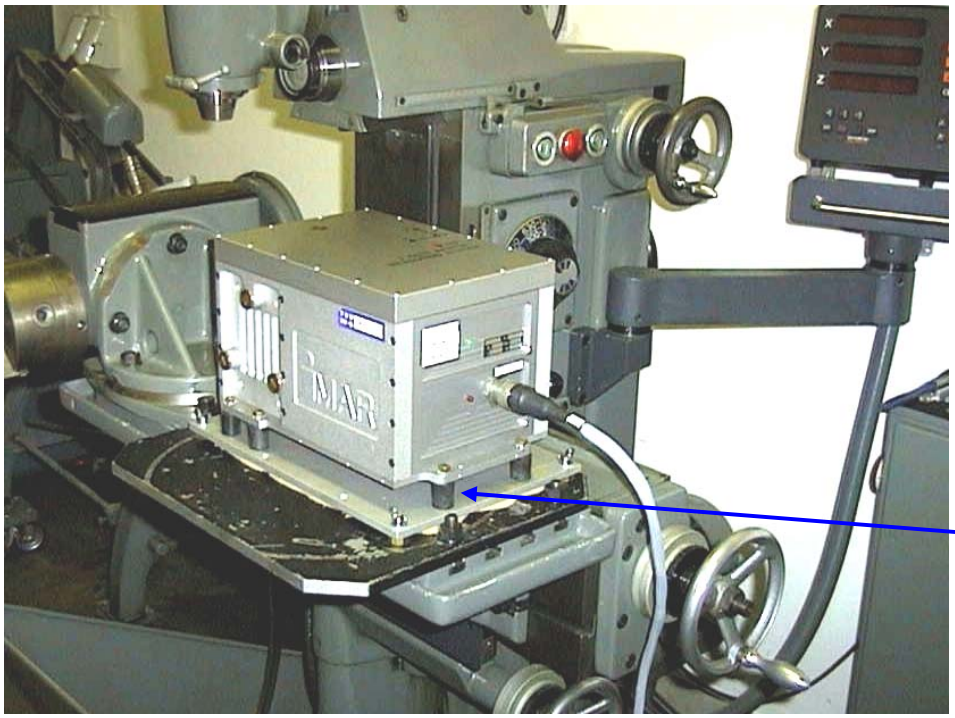

Fig. C-1 *IMU's mount using rubber-damper*

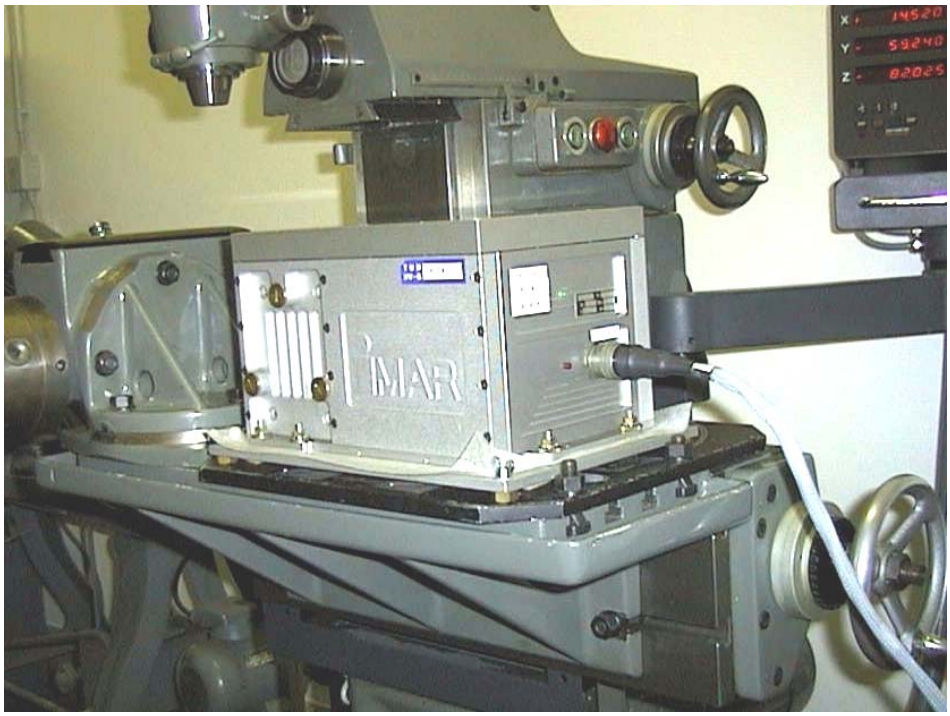

Fig. C-2 *Firm-fixing of the IMU*

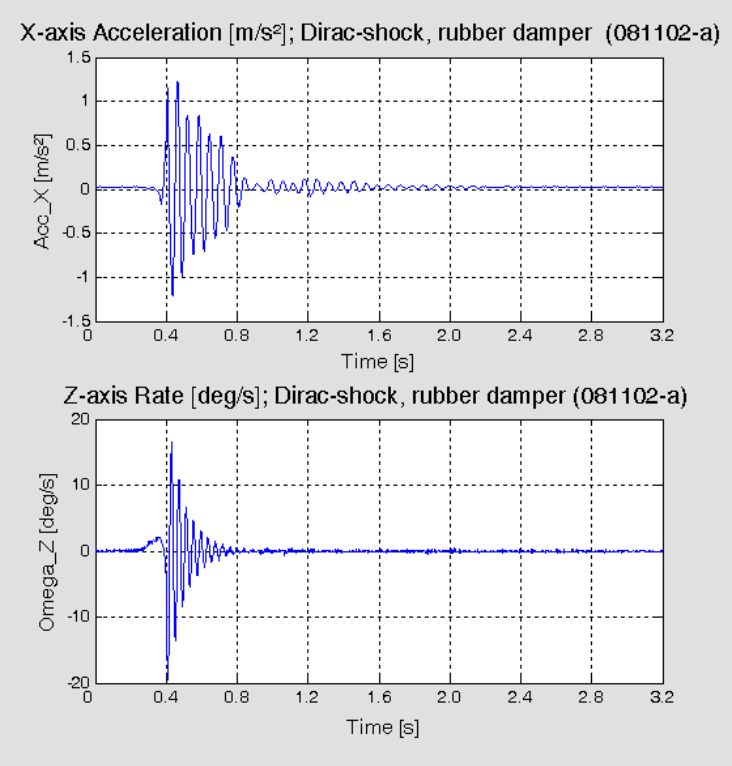

Fig. C-3 *Accelerometer and gyroscope response to a Dirac-shock, mechanical excitation applied to the IMU fixed with the six rubber-dampers (see Fig. **C-1**)*

For the graphical determination of the damping factor ξ we derived the relation (C-1) given below:

$$\xi = \frac{\ln \frac{\Delta A_{12}}{\Delta A_{23}}}{\sqrt{\pi^2 + \ln^2 \frac{\Delta A_{12}}{\Delta A_{23}}}}, \quad \text{(C-1)}$$

which uses the difference between the successive amplitude extremes:

$$\Delta A_{n,n+1} = A_{n+1} - A_n \quad \text{(C-2)}$$

(the formula is insensitive to eventually offsets present in the oscillation graphic).

So, we could estimate the global damping factors (sensor + IMU's internal shock-mounts + external rubber dampers) derived from the accelerometer, respectively gyro data (see Fig. C-3) to be about $\xi_{acc\_X} = 0.05$, resp. $\xi_{gyro\_Z} = 0.07$. These represent a quite low damping of the IMU's sensors, mainly due to the internal shock-mounts (that normally assure a good protection against accidentally shocks occurring during measurements or mounting of the unit).

Figure C-4 shows PSDs of the accelerometer measurements with/without external damping. In order to put into evidence the small differences between the two curves they are plotted twice, in different order (upper figure with external damping in the foreground resp. in the background in the lower figure). We observe a light increase of the signal around the resonance frequencies (the principal one situated at about 15 Hz), but the differences are quite small because of the effect of the cascaded mounting of the internal and external shock-mounts (the supplementary damping contribution of the external 6 rubber elements is hidden by the efficiency of the 8 internal damping elements).

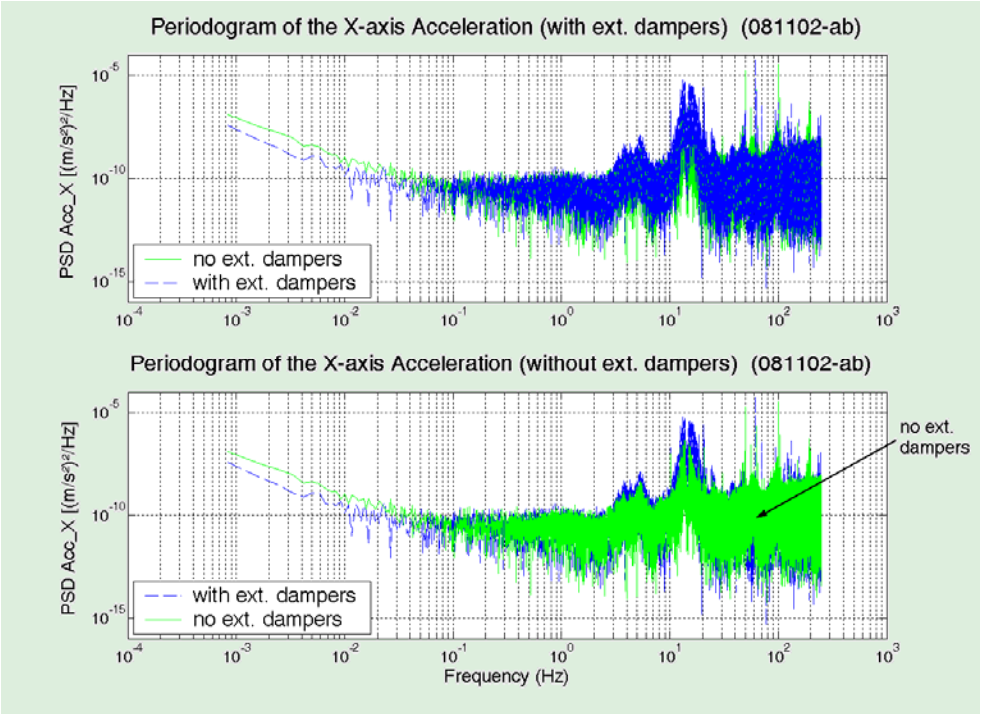

Fig. C-4 *PSD diagrams for the firm or rubber-dampers IMU's mounting*

Appendix D: **Some results from the direct use of the SIMU data-set for geodetic parameter determinations**

Using averaged series of data, a rough rapid gravity and earth rotation rate are computed, with the aim to quickly derive the **latitude**, the magnitude of the **earth rotation rate**, the **local gravity** and the **attitude**. Comparisons with precision external references are carried out: mean earth-rotation rate, precision absolute local gravimetry determination, precision GPS latitude measurement, Kalman-filtering attitude determinations (algorithm implemented on-line, on the SIMU, or in post-processing mode). The comparisons enable a rapid insight in the SIMU static sensitivity performance.
Some preliminary computations, usually made for the automated initialization of the strapdown algorithms, using the raw SIMU data, give also a further insight on the IMU's data precision. In the following steps we have adopted principally the derivations from *[Titterton, 1997]*, with the corresponding adaptation needed by the employment of the ENU local navigation system.
All these direct results are compared to the refined solutions of the Kalman filtering alignment estimations, computed on-line on the SIMU itself or off-line, by using the Kingspad post-processing software.
A typical 680 s static measurement sequence (100 Hz sampling rate) was considered (SIMU was first roughly horizontalized: the residual angles lie in the range of under 20 arcmin); during this time-period an on-line alignment process on the IMU was initialized (provided with Kalman filtering for the successive coarse and fine alignments, respectively). The fine-alignment solution (250402-b) was taken into consideration as reference (NRPY variable, which deliver the Roll, Pitch, Yaw Euler/Cartan angles *[Wertz, 1991]* by rotation from the *ENU Navigation-frame* to the *body reference-frame*) in comparison of the rough-estimated attitude and the fine-alignment.
The considered reference values are:

- earth rotation rate: $\Omega_E = 0.7292115085 \cdot 10^{-4}$ *rad/s (15.0410670514 deg/h)*
- local gravity: $g = 9.807254$ *m/s²* (Station 18/4 München, Technische Universität, Deutsches Schweregrundnetz *[Torge et al., 1999]*)
- latitude: $\varphi = 48°\ 09'\ 02.9''$ *N*
- longitude: $\lambda = 11°\ 34'\ 08.5''$ *E*
- height: *h = 510.87 m (DHHN 92)*
- roll, pitch, yaw: $\phi = 0.076$ *deg;* $\theta = 0.297$ *deg;* $\psi = -114.350$ *deg*

(the roll, pitch, yaw angles are taken from our.

1. Magnitude of the **earth rotation rate**

The magnitude of the earth rotation rate is independent from the SIMU's attitude. To calculate an estimation of the earth rotation rate, one considers the mean of the measured angle velocity components (SIMU's variable IOMG) over about 10 minutes:

$$\hat{\Omega}_E\ [\text{deg/h}] = 3600 \cdot \sqrt{(\overline{\omega}_x^b)^2 + (\overline{\omega}_y^b)^2 + (\overline{\omega}_z^b)^2}\ , \tag{D-1}$$

where the angle-hat signifies an estimated value, and the upper-line an averaged value.
The rotation rates body-components are computed directly from the gyros measurements (IOMG):

$$\boldsymbol{\omega}_{ie}^b = [\omega_x^b \quad \omega_y^b \quad \omega_z^b]^T\ . \tag{D-2}$$

The estimated value of earth rotation rate: $\hat{\Omega}_E = 15.0365$ deg/h approximate quite well the reference value of $\Omega_E = 15.041$ *deg/h*.

2. Local gravity

The magnitude of the local gravity is also independent from the IMU's attitude. We have estimated the gravity magnitude by using averaged values (over about 10 minutes) of the measured accelerations (each 0.01 s), that are components of the SIMU's variable IACC:

$$\hat{\mathrm{g}}\ [\mathrm{m/s^2}] = \sqrt{(\overline{a}_x^b)^2 + (\overline{a}_y^b)^2 + (\overline{a}_z^b)^2}\ . \tag{D-3}$$

where the body acceleration components are computed directly from the accelerometers specific force measurements (IACC):

$$\mathbf{a}^b = \left[\mathrm{a}_x^b \quad \mathrm{a}_y^b \quad \mathrm{a}_z^b\right]^T \tag{D-4}$$

The derived value $\hat{\mathrm{g}} = 9.8081$ approximates also quite well the reference value of the local gravity $g = 9.80725$ *m/s²*.

3. Latitude determination

The latitude is simply determined from the total horizontal component (along the N-axis of the ENU triad) of the earth rotation rate: $\boldsymbol{\omega}_{ie}^n = \left[0 \quad \Omega_E \cdot \cos\varphi \quad \Omega_E \cdot \sin\varphi\right]^T$, evaluated as the quadratic sum of the measured IMU's horizontal rates (under the assumption of the leveled SIMU). So, using the averaged values of the measured rates, over the same time duration of about 10 minutes, one estimate the latitude:

$$\hat{\varphi}\,[\text{deg}] = \frac{180}{\pi}\cdot \arccos\left(\frac{\sqrt{(\overline{\omega}_x^b)^2 + (\overline{\omega}_y^b)^2}}{\Omega_E}\right). \qquad \text{(D-5)}$$

The estimated value for the latitude is: $\hat{\varphi} = 47°\ \ 57'\ \ 29''$ (also quite close to the reference latitude of the experiment: $\varphi = 48°\ \ 09'\ \ 02.9''\ N$).

4. North-finding technique to determine the heading angle for the **leveled strapdown** system ($a_x^b = a_y^b = 0$)

Assuming a horizontalized system of two orthogonal gyroscopes and the yaw angle ψ_N between the north direction and the input-axis of the x-gyroscope, the measured angle rates are respectively:

$$\omega_x^b = \Omega_E \cdot \cos\varphi \cdot \cos\psi_N \qquad \text{(D-6)}$$

$$\omega_y^b = \Omega_E \cdot \cos\varphi \cdot \sin\psi_N, \qquad \text{(D-7)}$$

and so the estimated heading angle $\hat{\psi}_N$ is computed using the mean values of the gyros measurements:

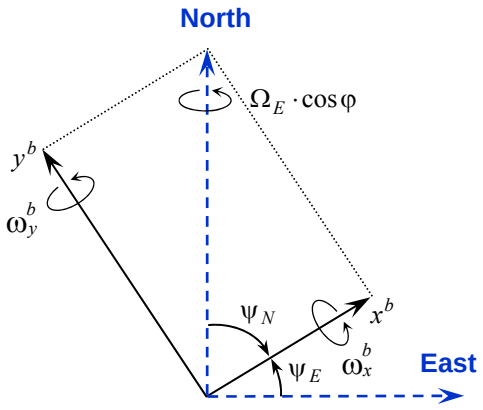

Fig. D-1 *North-finding technique for the levelled strapdown system*

$$\hat{\psi}_N = \arctan\frac{\overline{\omega}_y^b}{\overline{\omega}_x^b}. \qquad \text{(D-8)}$$

The north-referenced estimated value of the effective heading (*cw* from North direction in the NED right-frame), computed using a four-quadrant inverse tangent function (e.g., **atan2** from Matlab©, which delivers values in the interval $\psi_N \in (-180, 180)$ deg), is:

$$\hat{\psi}_N = -155.618 \text{ deg}$$

The east-referenced yaw-angle (*ccw* from East direction in the ENU right-frame), is determined as:

$$\hat{\psi}_E = 90 - \hat{\psi}_N = 245.618 \text{ deg},$$

which exprimed also with values in the interval $\psi_E \in (-180, 180)$ deg gives:

$$\psi_E = 245.618 - 360 = -114.382 \text{ deg},$$

that agrees quite well with the east-referenced fine-alignment solution: $\psi = -114.350$ *deg*.

5. Estimating the **pitch and roll** angles (ϕ, θ) for the stationary system **from accelerometer measurements**

Using the expression for the measured accelerations $\mathbf{a}^b$:

$$\mathbf{a}^b = -\mathbf{C}_n^b \cdot \mathbf{g}^n \qquad \text{(D-9)}$$

(where the minus sign comes from taking into account the equivalence between the gravity and acceleration (see Fig. 4.a)), or explicitly for the ENU reference system:

$$\mathbf{g}^n = \begin{bmatrix} 0 & 0 & -g \end{bmatrix}^T, \qquad \text{(D-10)}$$

and also expressing the transformation matrix $\mathbf{C}_n^b$ in terms of Euler angles (representation type 3-2-1: first rotation about the third axis "Up" through the yaw angle ψ, and so on: $\mathbf{C}_n^b = \mathbf{C}_1(\phi)\cdot\mathbf{C}_2(\theta)\cdot\mathbf{C}_3(\psi)$), adopting the evident symbols *s*, *c* for *sin*, *cos*, respectively *[Titterton, 1997]*:

$$\begin{bmatrix} a_x^b \\ a_y^b \\ a_z^b \end{bmatrix} = \begin{bmatrix} c\psi\cdot c\theta & s\psi\cdot c\theta & -s\theta \\ -s\psi\cdot c\phi + c\psi\cdot s\theta\cdot s\phi & c\psi\cdot c\phi + s\psi\cdot s\theta\cdot s\phi & c\theta\cdot s\phi \\ s\psi\cdot s\phi + c\psi\cdot s\theta\cdot c\phi & -c\psi\cdot s\phi + s\psi\cdot s\theta\cdot c\phi & c\theta\cdot c\phi \end{bmatrix} \cdot \begin{bmatrix} 0 \\ 0 \\ g \end{bmatrix}, \qquad \text{(D-11)}$$

the estimated *roll and pitch angles* $\hat{\phi}$, $\hat{\theta}$ are determined (using the mean-values of the acceleration components):

$$\hat{\phi} = \arctan\left(\overline{a}_y^b / \overline{a}_z^b\right) \qquad \text{(D-12)}$$

$$\hat{\theta} = \arcsin\frac{-\overline{a}_x^b}{\sqrt{\left(\overline{a}_x^b\right)^2 + \left(\overline{a}_y^b\right)^2 + \left(\overline{a}_z^b\right)^2}}. \qquad \text{(D-13)}$$

The computed values of $\hat{\phi} = 0.0810$ deg and $\hat{\theta} = 0.2967$ deg agree respectively well with the reference values of $\phi = 0.076$ *deg* and $\theta = 0.297$ *deg*.

The roll and pitch angles are estimated with an approximately accuracy equal to the accelerometer bias divided by gravity.

6-a. Strapdown platform **gyrocompass** (by stationary alignment)

With the assumed known vectors of local gravity and earth rotation rate, given in the ENU local-level system:

$$\mathbf{g}^n = \begin{bmatrix} 0 & 0 & -\mathrm{g} \end{bmatrix}^T \qquad \text{(see relation (D-10), repeated here for convenience)}$$

$$\boldsymbol{\omega}_{ie}^n = \begin{bmatrix} 0 & \Omega_E \cdot \cos\varphi & \Omega_E \cdot \sin\varphi \end{bmatrix}^T , \tag{D-14}$$

and the transformations:

$$\mathbf{a}^b = -\mathbf{C}_n^b \cdot \mathbf{g}^n \; ; \;\; \boldsymbol{\omega}_{ie}^b = \mathbf{C}_n^b \cdot \boldsymbol{\omega}_{ie}^n , \tag{D-15}$$

where the body components are computed directly from the statical measurements (D-2), (D-4). This gives (see, e.g., *[Titterton et al. (1997)]*, considering the ENU reference system in lieu of the NED one) for $\mathbf{C}_b^n(i, j)$, with i = 1…3, j = 1…3, elements of the matrix $\mathbf{C}_b^n = (\mathbf{C}_n^b)^T$ (denoting now $g_j^b = \mathrm{a}_j^b$ and considering mean-values for the measured specific forces (resulting from the **g**-input), respectively for the measured body-rates) the following estimations:

$$\hat{\mathbf{C}}_b^n(3,1) = \frac{\overline{g}_x^b}{g} \; ; \quad \hat{\mathbf{C}}_b^n(3,2) = \frac{\overline{g}_y^b}{g} \; ; \quad \hat{\mathbf{C}}_b^n(3,3) = \frac{\overline{g}_z^b}{g} \tag{D-16}$$

$$\hat{\mathbf{C}}_b^n(2,1) = \frac{\overline{\omega}_x^b}{\Omega_E \cdot \cos\varphi} - \frac{\overline{g}_x^b \cdot \tan\varphi}{g} ; \tag{D-17}$$

$$\hat{\mathbf{C}}_b^n(2,2) = \frac{\overline{\omega}_y^b}{\Omega_E \cdot \cos\varphi} - \frac{\overline{g}_y^b \cdot \tan\varphi}{g} ; \tag{D-18}$$

$$\hat{\mathbf{C}}_b^n(2,3) = \frac{\overline{\omega}_z^b}{\Omega_E \cdot \cos\varphi} - \frac{\overline{g}_x^b \cdot \tan\varphi}{g} . \tag{D-19}$$

One must observe, of course, the singularities of this procedure at the poles (North, South).

To compute the remaining terms of the rotation matrix $\mathbf{C}_b^n$ one uses the orthogonality property: the rows (resp. columns) constitute an orthonormal basis (each row has unity length, and the rows are mutually perpendicular).

So, one determines the remaining elements of $\mathbf{C}_b^n$ (the first row) as the vectorial product of the other two row-vectors:

$$\mathbf{C}_b^n(1,1) = \mathbf{C}_b^n(2,2) \cdot \mathbf{C}_b^n(3,3) - \mathbf{C}_b^n(2,3) \cdot \mathbf{C}_b^n(3,2) \tag{D-20}$$

$$\mathbf{C}_b^n(1,2) = -\mathbf{C}_b^n(2,1) \cdot \mathbf{C}_b^n(3,3) + \mathbf{C}_b^n(2,3) \cdot \mathbf{C}_b^n(3,1) \tag{D-21}$$

$$\mathbf{C}_b^n(1,3) = \mathbf{C}_b^n(2,1) \cdot \mathbf{C}_b^n(3,2) - \mathbf{C}_b^n(2,2) \cdot \mathbf{C}_b^n(3,1) \tag{D-22}$$

In fact, due to the orthogonality property of the transformation matrix $\mathbf{C}_b^n$, there are finally only three independent parameters, corresponding to the characterization of the unique Euler rotation-axis and of the rotation-angle about it.

The numerical values for the elements of the estimated rotation matrix $\hat{\mathbf{C}}_n^b$, the transpose of the computed $\hat{\mathbf{C}}_b^n$ matrix, are:

$$\hat{\mathbf{C}}_n^b = \begin{bmatrix} -0.412561 & -0.910022 & -0.005179 \\ 0.910029 & -0.412573 & 0.001414 \\ -0.003423 & -0.004002 & 0.999986 \end{bmatrix} . \tag{D-23}$$

One observes the perfect agreement with the estimation given below in the section 6-b (relation (D-28)).

6-b. An alternative method *[Farell et al. (1999)]* for the estimation of the **initial transformation matrix**

The rotation matrix $\mathbf{C}_n^b$ is determined from the transformation of a set of the three vectors (denoted **u**, **v**, **w**): $\mathbf{g}$, $\boldsymbol{\omega}$, $\mathbf{g} \times \boldsymbol{\omega}$, assumed known in the ENU *navigation* frame and measured in the *body* frame.

The transformation equation is:

$$[\mathbf{u}^b \quad \mathbf{v}^b \quad \mathbf{w}^b] = \mathbf{C}_n^b \cdot [\mathbf{u}^n \quad \mathbf{v}^n \quad \mathbf{w}^n] \tag{D-24}$$

i.e.:

$$\mathbf{C}_n^b = [\mathbf{u}^b \quad \mathbf{v}^b \quad \mathbf{w}^b] \cdot [\mathbf{u}^n \quad \mathbf{v}^n \quad \mathbf{w}^n]^{-1} \tag{D-25}$$

Taking for the gravity and earth rotation rates (see Fig. 16) the vectors from relations (D-10), (D-14), the transformation matrix has the explicit form (denoting with $\mathbf{a}^b$ and $\boldsymbol{\omega}^b$ the vectors of acceleration measurement in the body reference system, resp. the vector of rotation rate measurement in the same reference system):

$$\mathbf{C}_n^b = \begin{bmatrix} a_x^b & \omega_x^b & a_y^b \cdot \omega_z^b - a_z^b \cdot \omega_y^b \\ a_y^b & \omega_y^b & a_z^b \cdot \omega_x^b - a_x^b \cdot \omega_z^b \\ a_z^b & \omega_z^b & a_x^b \cdot \omega_y^b - a_y^b \cdot \omega_x^b \end{bmatrix} \cdot \begin{bmatrix} 0 & 0 & -g \cdot \Omega_E \cdot \cos\varphi \\ 0 & \Omega_E \cdot \cos\varphi & 0 \\ g & \Omega_E \cdot \sin\varphi & 0 \end{bmatrix}^{-1} \tag{D-26}$$

and so, the estimated initial rotation matrix:

$$\hat{\mathbf{C}}_n^b = \begin{bmatrix} \overline{a}_x^b & \overline{\omega}_x^b & \overline{a}_y^b \cdot \overline{\omega}_z^b - \overline{a}_z^b \cdot \overline{\omega}_y^b \\ \overline{a}_y^b & \overline{\omega}_y^b & \overline{a}_z^b \cdot \overline{\omega}_x^b - \overline{a}_x^b \cdot \overline{\omega}_z^b \\ \overline{a}_z^b & \overline{\omega}_z^b & \overline{a}_x^b \cdot \overline{\omega}_y^b - \overline{a}_y^b \cdot \overline{\omega}_x^b \end{bmatrix} \cdot \begin{bmatrix} 0 & -\frac{1}{g} \cdot \tan\varphi & \frac{1}{g} \\ 0 & \frac{1}{\Omega_E \cdot \cos\varphi} & 0 \\ -\frac{1}{g \cdot \Omega_E \cdot \cos\varphi} & 0 & 0 \end{bmatrix}, \tag{D-27}$$

where for the body components of specific force, resp. rotation rates (given in relations (D-2), (D-4)) were considered the mean-values for the static measurements during the above 10 minutes of alignment phase.
Of course, one must observe the *singularities* of this procedure *at the poles (N, S).*
Taking averaged values for the measured components of the body specific forces and angular rates, and also the reference values for the earth rotation rate, local gravity and latitude, the estimated transformation matrix $\hat{\mathbf{C}}_n^b$ reads in numerical form:

$$\hat{\mathbf{C}}_n^b = \begin{bmatrix} -0.412561 & -0.910022 & -0.005179 \\ 0.910029 & -0.412573 & 0.001414 \\ -0.003423 & -0.004002 & 0.999986 \end{bmatrix} \tag{D-28}$$

One observes the sub-unitary values of that matrix of cosine-direction terms, a first indication of the numerical correctness (compare also with the matrix in D-23).

6-c. Checking the **consistence** for the computed transformation matrix

Self consistency tests for the orthonormal transformation matrix $\mathbf{C}_n^b$ – check for their orthogonality (scalar products of arbitrary row- and a column-vectors must be null) and normality (sum of the squares of the row-elements must be unitary) – and attempts to reduce the respective errors, by applying appropriate corrections, is a common practice in the development of strapdown mechanization software. The main causes for this type of errors are the initialization errors or the round-off errors occurring at each update in the strapdown algorithm.

Using a simplified notation to explicit the relation between the erroneous transformation matrix $\hat{\mathbf{C}}$ and the idealized error-free transformation matrix $\mathbf{C}$:

$$\hat{\mathbf{C}} = (\mathbf{I} + \mathbf{E}) \cdot \mathbf{C}, \tag{D-29}$$

with:

$\mathbf{I}$ = identity matrix
$\mathbf{E}$ = error matrix

and putting into evidence the decomposition of $\mathbf{E}$ in the symmetric (orthogonality and normality errors) and skew symmetric (misalignment errors) components:

$$\mathbf{E} = \mathbf{E}_{SYM} + \mathbf{E}_{SKSYM}, \tag{D-30}$$

one deduce *[Savage, 2000]*, after neglecting of the second order terms, the expression of the symmetric part:

$$\mathbf{E}_{SYM} = \frac{1}{2} \cdot (\hat{\mathbf{C}} \cdot \hat{\mathbf{C}}^T - \mathbf{I}). \tag{D-31}$$

Therewith, the algorithm for correcting orthogonality/normality errors is *[Savage, 2000]*:

$$\hat{\mathbf{C}}_+ = (\mathbf{I} - \mathbf{E}_{SYM}) \cdot \hat{\mathbf{C}}_- \tag{D-32}$$

with:

$\hat{\mathbf{C}}_+$ = transformation matrix value after the correction

$\hat{\mathbf{C}}_-$ = transformation matrix value before the correction.

Applying the correction algorithm to the transformation matrix numerically given in relation (D-28) we get the corrected form:

$$(\hat{\mathbf{C}}_n^b)_+ = \begin{bmatrix} -0.412897 & -0.910762 & -0.005121 \\ 0.910770 & -0.412909 & 0.001440 \\ -0.003426 & -0.004069 & 0.999986 \end{bmatrix} \tag{D-33}$$

The corresponding orthogonality/normality errors for the original and corrected transformation matrix are respectively:

$$(\mathbf{E}_{SYM})_{-} = 10^{-3} \cdot \begin{bmatrix} -0.813692 & 0.000048 & -0.062164 \\ 0.000048 & -0.814387 & -0.025121 \\ -0.062164 & -0.004002 & -0.999986 \end{bmatrix} \quad \text{(D-34)}$$

and

$$(\mathbf{E}_{SYM})_{+} = 10^{-6} \cdot \begin{bmatrix} -0.999484 & -0.002227 & -0.075963 \\ -0.002227 & -0.996327 & -0.030719 \\ -0.075963 & -0.030719 & -0.006747 \end{bmatrix} \quad \text{(D-35)}$$

We can see the dramatically improvement of the matrix orthonormality (most of the errors are diminished about 1000 times). In the product of the corrected form of the transformation matrix with its transpose one observes the closeness to the identity matrix and also the perfect symmetry of the small off-diagonal terms:

$$(\hat{\mathbf{C}}_n^b)_{+} \cdot (\hat{\mathbf{C}}_n^b)_{+}^T = \begin{bmatrix} 0.99999800103190 & -0.00000000445445 & -0.00000015192619 \\ -0.00000000445445 & 0.99999800734634 & -0.00000006143889 \\ -0.00000015192619 & -0.00000006143889 & 0.99999998650575 \end{bmatrix} \quad \text{(D-36)}$$

Nevertheless, the correction being somewhat arbitrary (e.g., the orthogonality error is assumed equally distributed between the orthogonal matrix rows), a supplementary check of the final solution consistency is always necessary.

6-d. Deriving of the **Euler angles** from the computed rotation matrix

Using the explicit relation of the $\mathbf{C}_n^b$ from (D-11), we can derive the three Euler-angles using the coefficients of the estimated transformation matrix, which gives the following estimations:

The Pitch angle: $\hat{\theta}\,[\text{deg}] = -\arcsin(\hat{\mathbf{C}}_n^b(1,3)) \cdot \dfrac{180}{\pi}$

$= 0.297$ deg

The Roll angle: $\hat{\phi}\,[\text{deg}] = \arccos(\hat{\mathbf{C}}_n^b(3,3) / \cos\hat{\theta}) \cdot \dfrac{180}{\pi}$

$= 0.081$ deg

The Yaw angle: $\hat{\psi}\,[\text{deg}] = \pm\arccos(\hat{\mathbf{C}}_n^b(1,1) / \cos\hat{\theta}) \cdot \dfrac{180}{\pi}$

$= -114.366$ deg (for the actual angle in quadrant III),

all of them in a very good concordance with the NRPY reference values resulted after the SIMU's fine alignment ($\phi = 0.076$ deg; $\theta = 0.297$ deg; $\psi = -114.350$ deg).

6-e. Alternative Least-Square method for the estimation of the **initial transformation matrix**

An adjustment solution for the transformation (rotation) matrix could be obtained also through a least-squares approach *[Hofmann-Wellenhof et al., 2003]*. The matriceal form of the least squares solution is:

$$\hat{\mathbf{C}}_n^b = \left[\mathbf{a}^b \quad \boldsymbol{\omega}^b \quad \mathbf{a}^b \times \boldsymbol{\omega}^b\right] \cdot \left[\mathbf{g}^n \quad \boldsymbol{\omega}_{ie}^n \quad \mathbf{g}^n \times \boldsymbol{\omega}_{ie}^n\right]^T \cdot \left(\left[\mathbf{g}^n \quad \boldsymbol{\omega}_{ie}^n \quad \mathbf{g}^n \times \boldsymbol{\omega}_{ie}^n\right] \cdot \left[\mathbf{g}^n \quad \boldsymbol{\omega}_{ie}^n \quad \mathbf{g}^n \times \boldsymbol{\omega}_{ie}^n\right]^T\right)^{-1} \quad \text{(D-37)}$$

However, this relation is more difficult to implement (because of the large measurement matrices sizes: 60,000 values for 10 minutes static alignment at a sampling rate of 100 Hz) compared to the direct use of the measurement mean-values in the alignment transformation matrix estimation from eq. (D-27).

Veröffentlichungen in der Schriftenreihe IAPG / FESG (ISSN 1437-8280):
Reports in the series IAPG / FESG (ISSN 1437-8280):

No. 1: Müller J., Oberndorfer H. (1999). *Validation of GOCE Simulation.* ISBN 3-934205-00-3.

No. 2: Nitschke M. (1999). SATLAB – *Ein Werkzeug zur Visualisierung von Satellitenbahnen.* ISBN 3-934205-01-1.

No. 3: Tsoulis D. (1999). *Spherical harmonic computations with topographic/isostatic coefficients.* ISBN 3-934205-02-X.

No. 4: Dorobantu R. (1999). *Gravitationsdrehwaage.* ISBN 3-934205-03-8.

No. 5: Schmidt R. (1999). *Numerische Integration gestörter Satellitenbahnen mit* MATLAB. ISBN 3-934205-04-6.

No. 6: Dorobantu R. (1999). *Simulation des Verhaltens einer low-cost Strapdown-IMU unter Laborbedingungen.* ISBN 3-934205-05-4.

No. 7: Bauch A., Rothacher M., Rummel R. (2000). *Bezugssysteme in Lage und Höhe. Tutorial zum Kursus INGENIEURVERMESSUNG 2000.* ISBN 3-934205-06-2.

No. 8: Rothacher M., Zebhauser B. (2000). *Einführung in GPS. Tutorial zum 3. SAPOS-Symposium 2000 in München.* ISBN 3-934205-07-0.

No. 9: Ulrich M. (2000). *Vorhersage der Erdrotationsparameter mit Hilfe Neuronaler Netze.* ISBN 3-934205-08-9.

No. 10: Seitz F. (2000). *Charakterisierung eines bistatischen Rayleigh- und Raman-Lidars zur Bestimmung von höhenaufgelösten Wasserdampfprofilen.* ISBN 3-934205-09-7.

No. 11: Meyer F. (2000). *Messung von höhenaufgelösten Wasserdampfprofilen unter Verwendung eines bistatischen Raman-Lidars.* ISBN 3-934205-10-0.

No. 12: Peters T. (2001). *Zeitliche Variationen des Gravitationsfeldes der Erde.* ISBN 3-934205-11-9.

No. 13: Egger D. (2001). *Astronomie und Java – Objekte der Astronomie.* ISBN 3-934205-12-7.

No. 14: Steigenberger P. (2002). MATLAB-*Toolbox zur TOPEX/POSEIDON Altimeterdatenverarbeitung.* ISBN 3-934205-13-5.

No. 15: Schneider M. (2002). *Zur Methodik der Gravitationsfeldbestimmung mit Erdsatelliten.* ISBN 3-934205-14-3.

No. 16: Dorobantu R., Gerlach C. (2004). *Investigation of a Navigation–Grade RLG SIMU type iNAV–RQH.* ISBN 3-934205-15-1.

Weitere Exemplare können bezogen werden unter:
Copies are available from:
Institut für Astronomische und Physikalische Geodäsie
Technische Universität München
Arcisstrasse 21
D-80290 München
Germany
Telefon: +49-89-289-23190
Telefax: +49-89-289-23178
Email: gerlach@bv.tum.de

Oder im Internet:
Or via Internet:
http://tau.fesg.tu-muenchen.de/~iapg/web/veroeffentlichung/schriftenreihe/schriftenreihe.php

ISSN 1437-8280, ISBN 3-934205-15-1